Volume 12 | Number 23 | 7 December 2025

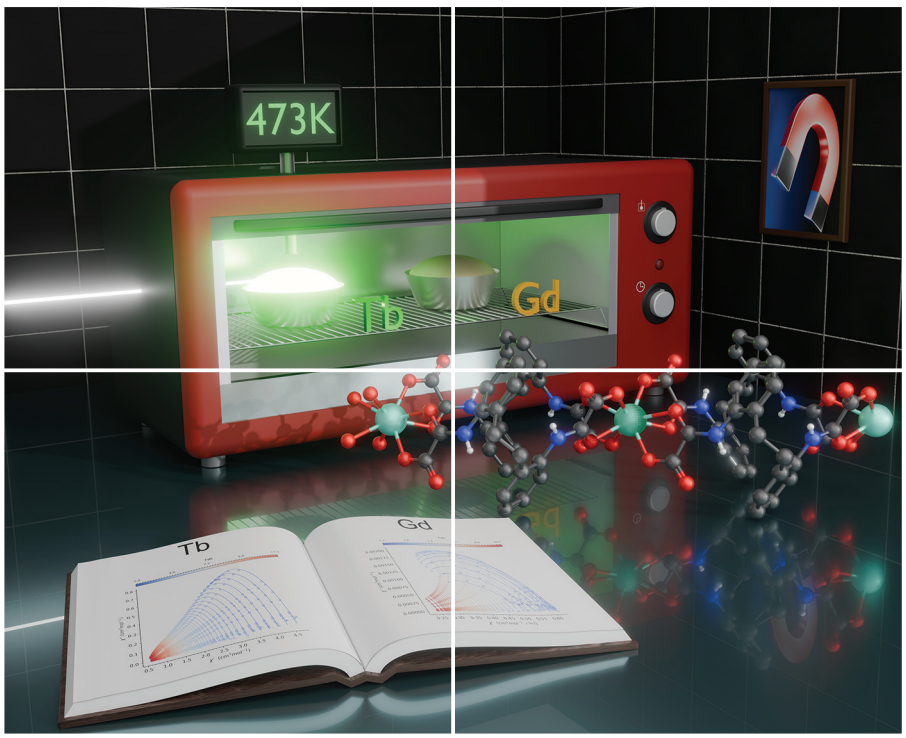


# INORGANIC CHEMISTRY

## FRONTIERS

CCS 中国化学会 CHINESE CHEMICAL SOCIETY
PEKING UNIVERSITY 1898
ROYAL SOCIETY OF CHEMISTRY
rsc.li/frontiers-inorganic

INORGANIC CHEMISTRY FRONTIERS

RESEARCH ARTICLE

View Article Online
View Journal | View Issue



Cite this: *Inorg. Chem. Front.*, 2025, **12**, 7512

# Reciprocating thermal behavior and thermometry studies of $Tb^{3+}$- and $Gd^{3+}$-oxamato single-ion magnets

Cleber R. Araujo Junior, [a] Luana M. Murad, [a] Rafael V. Perrella, [b] Willian X. C. Oliveira, [a] Carlos B. Pinheiro, [c] Thais F. Ramos, [d] Patrícia S. O. Patricio, [d] Emerson F. Pedroso, [d] Wallace C. Nunes, [e] Pablo R. T. Ribeiro, [f] Diego Muraca, [f] Fernando Fabris, [f] Marcelo Knobel, [f] Fernando A. Sigoli [b] and Cynthia L. M. Pereira *[a]

Single-ion magnets (SIMs) are prominent candidates for promoting new technologies in quantum information processing (QIP). Herein, we present two new isostructural oxamato derivatives, namely, $\{n\text{-Bu}_4\text{N}[\text{Ln}(\text{H}_2\text{edpba})_2]\}_n$, Ln = $Tb^{3+}$ (**1**) and $Gd^{3+}$ (**2**) [$H_2edpba^{2-}$ = *N*,*N*′-2,2′-ethylenediphenylenebis(oxamate)], that are thermostable up to ~290 °C. Single-crystal X-ray diffraction reveals that **1** and **2** are one-dimensional coordination polymers with a ribbon-like structure, and their metal centers are eight-coordinated with a $D_{4d}$ symmetry. Cryomagnetic studies disclose the presence of slow magnetic relaxation (SMR) behavior for **1** and **2**. For **1**, the Raman effect dominates the SMR at a zero magnetic field, while Raman, Orbach, and reciprocating thermal behavior (RTB) mechanisms arise at higher fields. Conversely, RTB and the bottleneck effect were observed at **2**. Solid-state photoluminescent data display a remarkable green luminescence emission, with intense and sharp bands ranging from 480 to 700 nm in the spectra, which are attributed to the $^5D_4 \rightarrow {}^7F_J$ ($J$ = 6–0) transitions of terbium(III) ions. By monitoring the temperature-dependent lifetime of the $^5D_4$ state after the intensity decay of the emission band attributed to the $^5D_4 \rightarrow {}^7F_5$ (546 nm) transition, the complex shows a reasonable thermometric performance with a relative sensitivity of 2.77% $K^{-1}$ at 448 K. **1** behaves as a zero-field SIM and as a photoluminescent thermometer.

Received 31st July 2025,
Accepted 24th September 2025

DOI: 10.1039/d5qi01603g

rsc.li/frontiers-inorganic



## 1. Introduction

Lanthanide-based coordination compounds have emerged as a focal point of contemporary research due to their remarkable potential in molecular magnetism and photoluminescence.[1–3] In the context of magnetism, the strategic design of single-ion magnets (SIMs) through the coordination of lanthanide ions with tailored organic ligands has garnered intense interest, particularly owing to their applicability in cutting-edge quantum technologies.[4,5] These technologies harness the unique spin-dependent magnetic properties of such systems to enable transformative advancements in ultra-high-density data storage, quantum computing, spintronics, and quantum information processing (QIP).[6,7]

Nowadays, understanding the factors that affect magnetic properties, mainly the slow magnetic relaxation (SMR) phenomena that occur with several molecules and ions, are crucial for moving toward a potential device for QIP. Thus, discussing the spin-vibration phonon and spin-phonon mechanisms in the solid state and associating them with the crystalline structures is a strategy to increase knowledge and to reach a fundamental comprehension of all the factors that should be controlled to obtain a compound of interest.[8]

There are very few examples of terbium(III) complexes as zero-field SIMs in the literature.[9,10] The main reason is that the $Tb^{3+}$ ion is a non-Kramer ion (integer total spin value), *i.e.*, the SMR phenomenon is not expected without applying a static magnetic field. When the SMR is observed at a zero field, it is likely due to the combination of a favorable crystal field environment and hyperfine interactions.[11] In this regard, there are ideal point groups, such as $C_{\infty v}$, $D_{4d}$, $S_8$, $D_{5h}$, $D_{6d}$,

[a]*Departamento de Química, Universidade Federal de Minas Gerais, Av. Antônio Carlos 6627, Belo Horizonte, MG, 31270-901, Brazil. E-mail: cynthialopes@ufmg.br*
[b]*Departamento de Química Inorgânica, Instituto de Química, Universidade Estadual de Campinas, Campinas, SP, 13083-970, Brazil*
[c]*Departamento de Física, Universidade Federal de Minas Gerais, Av. Antônio Carlos 6627, Belo Horizonte, MG, 31270-901, Brazil*
[d]*Centro Federal de Educação Tecnológica de Minas Gerais, Belo Horizonte, MG, 30421-169, Brazil*
[e]*Instituto de Física, Universidade Federal Fluminense, Niterói, RJ, 24210-346, Brazil*
[f]*Instituto de Física Gleb Wataghin, Universidade Estadual de Campinas, Campinas, SP, 13083-859, Brazil*

and $D_{\infty h}$, that could suppress the unwanted quantum tunneling process, which favors SMR.[12]

In the case of gadolinium(III) complexes, although the number of works reporting SMR in these compounds is increasing, the number of reported examples is still quite scarce.[13,14] Gadolinium(III) is considered an isotropic ion ($4f^7$, $S = 7/2$, $L = 0$), *i.e.*, it displays a very low magnetic anisotropy with a general zero-field splitting parameter ($D$) of ~0.1 $cm^{-1}$, which accounts for very small double-well energy barriers of around 1 $cm^{-1}$ (calculated as $DS^2 - 1/4$, being $S = 7/2$) for the reversal of magnetization. Therefore, the observation of the SMR in gadolinium(III) complexes cannot be explained in terms of the suppression of quantum tunnelling of the magnetization (QTM) or due to an over-barrier process mechanism occurring in conventional SIMs.[13] Additionally, the environment around the lanthanide ion can be distorted by its interaction with ligands, which modifies its symmetry, mainly in low coordination numbers (8–11), resulting in a mix of low-lying states. In such a case, when an external magnetic field is applied, the degeneracy between energy levels can be removed, and the QTM can be suppressed, resulting in mixed mechanisms, such as spin–lattice, spin–phonon, and spin–spin relaxations, which account for the observation of SMR.[14,15]

Regarding luminescent properties of lanthanide-based coordination compounds, they exhibit sharp, long-lived (micro- and milli-second), and highly intense emissions, which span from the ultraviolet (UV) to the near-infrared (NIR) region, depending on the selected activator ion.[16] Among them, $Tb^{3+}$ is of particular interest owing to its intense green emission, which has been explored for remote temperature sensing.[17–19] This application has gained increasing relevance in microelectronics, microfluidics, SMM, and nanomedicine, where precise thermal monitoring at the micro- and nanoscale is essential.[20–23]

Two luminescence-based $Tb^{3+}$ thermometric approaches have effectively achieved reliable temperature readouts: emission lifetime measurements and the single-band ratiometric (SBR) method.[24–27] The emission lifetime is an intrinsic property of the luminescent thermometer because it directly reflects the electronic de-excitation kinetics, which are predominantly dictated by temperature and the dielectric properties of the surrounding medium.[28] Alternatively, the SBR method relies on the intensity ratio of a single emission band upon excitation at two distinct wavelengths, offering simplified temperature calibration due to its ratiometric nature.[25] In addition, as signals are detected within the same spectral window, this approach minimizes errors associated with variations in medium transmittance while reducing system complexity.[18,29]

Herein, we present the cryomagnetic and photophysical properties of two one-dimensional coordination polymers with formulas of $\{n\text{-}Bu_4N[Tb(H_2edpba)_2]\}_n$ (**1**) and $\{n\text{-}Bu_4N[Gd(H_2edpba)_2]\}_n$ (**2**); [$H_2edpba^{2-}$ = *N*,*N*′-2,2′-ethylenediphenylenebis(oxamate)]. **1** and **2** are the first examples of lanthanide(III) complexes with flexible $H_4edpba$ oxamic acid derivatives. Single crystals of **1** and **2** suitable for X-ray diffraction experiments were grown at room temperature in an open-air atmosphere under mild conditions. The results reveal that both terbium(III) and gadolinium(III) ions are magnetically isolated in the ribbon-like chain, displaying the idealized symmetry $D_{4d}$. **1** exhibits the SMR phenomena at zero and nonzero applied fields until 17 K ($H_{dc}$ = 500 Oe), which is the highest value for the terbium(III)-oxamato complex to date. Our findings offer insights into the influence of ligand design on magnetic properties and lanthanide luminescence and pave the way for the development of advanced lanthanide-based coordination polymers with multifunctional properties applicable to photonics, sensing, and quantum technologies.

## 2. Experimental

### 2.1. Materials and methods

All chemicals were of analytical grade and were used without further purification. The ethyl ester $Et_2H_2edpba$ proligand used in this work was synthesized as described previously.[30] Elemental analyses were performed using a PerkinElmer 2400 analyzer. IR spectra were recorded on KBr pellets in the 4000–400 $cm^{-1}$ range using a PerkinElmer 882 spectrophotometer. The thermal study (TG/DTA, thermogravimetric/differential thermal analysis) was performed with a DTG-60H using 4.76 mg ($4.3 \times 10^{-3}$ mmol) of the complex placed in an alumina crucible. The solid sample was heated at 10 K $min^{-1}$ from room temperature to 873 K under a $N_2$ atmosphere (flow rate = 50 ml $min^{-1}$). Differential scanning calorimetry (DSC) analysis was conducted using a PerkinElmer DSC 4000 instrument, with a sample of 5.00 mg ($4.50 \times 10^{-3}$ mmol) of **1** and 6.23 mg ($5.64 \times 10^{-3}$ mmol) of **2**, and indium as the reference material. Single-crystal X-ray diffraction (SCXRD) data collection was analyzed using a Rigaku Synergy diffractometer with Cu-Kα radiation (1.54184 Å) at 220 K. Data integration and scaling of the reflections for the SCXRD experiments were performed using the CRYSALIS suite.[31] The final unit cell parameters were based on fitting all reflection positions. Analytical absorption corrections and space group identification were performed using the CRYSALIS suite.[31] The crystalline structures of all compounds were solved using direct methods with the SUPERFLIP program.[32] The positions of all atoms can be unambiguously assigned to consecutive difference Fourier maps. Refinements were performed using SHELXL[33] based on $F^2$ using the full-matrix least-squares routine. All non-hydrogen atoms in the terbium(III) coordination polymer were refined using anisotropic atomic displacement parameters. The *n*-tetrabutylammonium cation is found over several symmetry elements of the crystallization space group and is dramatically disordered. The disorder was treated by dividing one of the *n*-butyl groups into two positions to better suit the electron density around the nitrogen atom. Additionally, as part of the disorder treatment, the geometric parameters (bond length and bond angles) for all bonds in this cation were restricted. Fig. S1 shows the asymmetric units of all compounds, highlighting the ellipsoids. The hydrogen atoms were included as

fixed contributions according to the riding model.[34] The fixed bond lengths and the isotropic atomic displacement for hydrogen atoms are as follows: C–H = 0.93 Å and $U_{iso}$(H) = 1.2 $U_{eq}$(C) for the aromatic carbon atoms, amide groups, C–H = 0.97 Å and $U_{iso}$(H) = 1.5 $U_{eq}$(C) for methyl groups, C–H = 0.97 Å and $U_{iso}$(H) = 1.2 $U_{eq}$(C) for methylene carbon atoms and N–H = 0.86 Å and $U_{iso}$(H) = 1.2 $U_{eq}$(N) for the amide groups. Figures were obtained using Mercury® software[35] and Vesta.[36] The crystal structure data were deposited with the Cambridge Crystallographic Data Center (CCDC) code at the end of Table S1.

The X-ray powder diffraction patterns (PXRDs) of **1** and **2** were recorded on an Empyrean (Panalytical) using CuKα radiation ($\lambda$ = 1.54056 Å). Simulated PXRD patterns were generated using Mercury® software[35] based on the crystal data obtained from the SCXRD CIF files of **1** and **2**. Variable-temperature static (dc) magnetic susceptibility and variable-field magnetization measurements were conducted using a Quantum Design SQUID magnetometer model MPMS-XL-5. For the variable-temperature dynamic (ac) magnetic susceptibility measurements, a Quantum Design PPMS-9 was utilized, operating with a small amplitude ac field (5 Oe) and scanning within a frequency range of 10 Hz–10 kHz under different applied dc magnetic fields. Both dc and ac magnetic measurements were performed on powdered polycrystalline samples, which were previously placed in gelatin capsules with mineral oil to prevent crystal movement. Corrections for the diamagnetism of the sample and sample holder were considered.

Luminescence spectra were collected on a Fluorolog 3 (Horiba FL3-22-iHR320) spectrofluorometer equipped with double-grating (1200 g $mm^{-1}$) monochromators blazed at 330 nm (excitation) and 500 nm (emission). A Hamamatsu R928P photomultiplier tube was employed as a detector, and a 450 W xenon arc lamp was used as the radiation source. The luminescence spectra were corrected for lamp intensity, optical response, and detector sensitivity using the software. The temperature-dependent complex **1** powder spectra were obtained between 77 and 473 K using a Linkam Scientific temperature-controlled stage (THMS600). Samples were thermalized (±0.1 K) for ~10 min before each measurement at the selected temperatures. The time-resolved phosphorescence spectra were collected at 77 K, applying different time delays for detection. Emission decay curves were collected using the same instrument with a TCSPC system and a 150 W xenon pulsed lamp as the excitation source.

### 2.2. Synthesis

**Syntheses of 1 and 2.** Compounds **1** and **2** were obtained using the same synthetic procedure through the *in situ* hydrolysis of the ethyl ester $Et_2H_2$edpba with *n*-$Bu_4NOH$. A mixture was prepared using $Et_2H_2$edpba (480 mg, 1.16 mmol), which was mixed in deionized water (30 mL), and tetrabutylammonium hydroxide (40 wt%, 1.33 mL, 2.05 mmol) was added to this mixture dropwise under continuous stirring and then maintained at 80 °C for 30 min. After hydrolysis, the mixture was cooled to room temperature, and DMSO (30 mL) was added dropwise. Then, an aqueous solution (6.0 mL) containing $TbCl_3 \cdot 6H_2O$ (0.62 mmol) was added dropwise under continuous stirring. Subsequently, the reaction mixture was heated for 15 min while maintaining the temperature at 80 °C. The resulting solution was filtered, and the filtrate was allowed to rest at 40 °C for subsequent crystallization. Single crystals were formed after 48 h. Colorless hexagonal prism crystals of **1** were obtained. **1** was suitable for the single-crystal X-ray diffraction experiment. $\{n\text{-}Bu_4N[Tb(edpba)_2]\}_n$ (**1**). Yield: 64% (362 mg; 0.362 mmol). IR (KBr, $cm^{-1}$): 3320 ($\nu_{N-H}$); 3079, 2964, 2872 ($\nu_{C-H}$); 1672, 1654 ($\nu_{C=O}$); 1529, 1484 ($\nu_{C=C}$); 840, 754 ($\gamma_{C-H}$) $cm^{-1}$. Elemental analysis (calcd.) for $C_{52}H_{64}TbN_5O_{12}$ (1110.00 g $mol^{-1}$): C 56.03 (56.27), H 5.86 (5.81), N 6.27 (6.31) %.

Compound **2** was synthesized using the same methodology described for **1**. The only difference is using Gd $(CH_3COO)_3 \cdot H_2O$ (0.55 mmol) salt instead of the terbium(III) one. $\{n\text{-}Bu_4N[Gd(edpba)_2]\}_n$ (**2**). Yield: 57% (365 mg; 0.329 mmol). IR (KBr, $cm^{-1}$): 3317 ($\nu_{N-H}$); 3079, 2965, 2936, 2875 ($\nu_{C-H}$); 1681, 1647 ($\nu_{C=O}$); 1529, 1482 ($\nu_{C=C}$); 852, 800 ($\gamma_{C-H}$) $cm^{-1}$. Elemental analysis (calcd) for $C_{52}H_{64}GdN_5O_{12}$ (1108.36 g $mol^{-1}$): C 56.19 (56.35), H 5.78 (5.82), N 6.28 (6.32) %.

## 3. Results and discussion

The synthetic procedure followed a one-pot synthesis approach, in which the proligand $Et_2H_2$edpba and *n*-$Bu_4NOH$ were used in a diluted DMSO solution to obtain the compound (Scheme 1), contrasting with other previous reports where the tetrabutylammonium salt was isolated, characterized, and subsequently added to the metal salt solution.[37,38] The used procedure was almost similar to those recently reported for the erbium(III)-oxamato calixarene-like complex.[39] However, the solvent temperatures differ. The first crystals appeared two

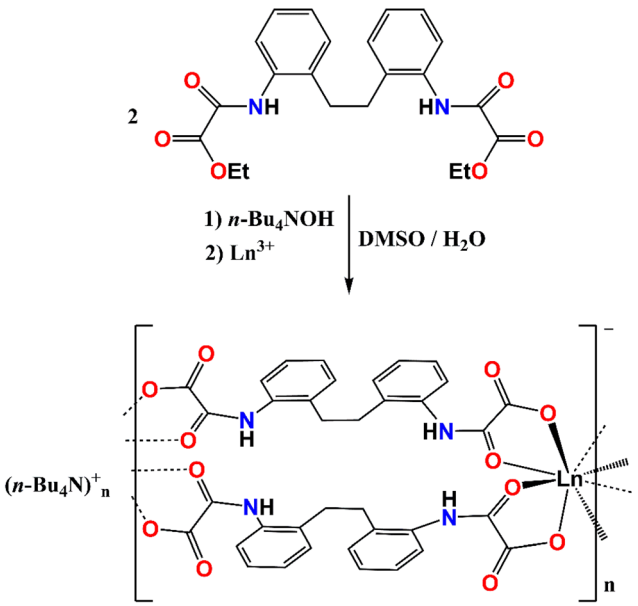


**Scheme 1** Schematic of the syntheses of the anionic coordination polymers **1** and **2**.

days after the synthesis and were collected five days later. It is worth noting that **1** is the first example of a lanthanide compound with *N*,*N*′-2,2′-ethylenediphenylenebis(oxamic acid) reported in the literature. Therefore, various structures with transition metals based on $Et_2H_2$edpba proligand have been published, ranging from monometallic to bimetallic and heterobimetallic complexes.[40–42]

Elementary analysis, the FT-IR spectra (Fig. S2 and S3), thermal analysis (Fig. S4 and S5) and differential scanning calorimetry analysis (Fig. S6 and S7) support the identity of **1** and **2**. At the same time, single-crystal X-ray diffraction (SCXRD) also confirms the stoichiometry of the structure (Fig. S8 and S9). By analyzing the FT-IR spectrum, the intense absorption bands observed at 2964 and 2872 $cm^{-1}$ are characteristics of the C–H stretching bonds from *n*-$Bu_4N^+$ groups. Additionally, the stretching vibrations of protonated amide N–H groups are observed at 3320 $cm^{-1}$. The downward shifting of the stretching vibrations of C=O groups (1672 and 1654 $cm^{-1}$) relative to the proligand $Et_2H_2$edpba (1733 and 1706 $cm^{-1}$)[30] is strong evidence of ester hydrolysis and further coordination with terbium(III) ions. It is also worth noting that these C=O bands may be coupled with the C=C stretching vibrations of the aromatic rings, which typically appear in the same region. Bands in the 1300–1000 $cm^{-1}$ range are assigned to the C–O and C–N stretching modes and in-plane aromatic ring deformations. The out-of-plane bending modes of aromatic C–H groups are also detected between 850 and 700 $cm^{-1}$, which is consistent with *ortho*-disubstituted benzene rings. Finally, the absorption band observed at approximately 490 $cm^{-1}$ is attributed to Ln–O stretching, confirming the coordination of the carboxylate oxygen atoms to the terbium(III) centers.

Thermal analyses (TG/DTA) for **1** and **2** (Fig. S4 and S5) confirm the absence of solvent molecules, as the molecular formula proposed by elemental analysis and SCXRD. **1** and **2** exhibit excellent thermal stability for an oxamato complex, as the compound mass remains constant upon heating up to approximately 286 °C (**1**) and 290 °C (**2**). Heating the sample causes decomposition through the release of oxamate groups. The differential scanning calorimetry analysis (DSC analysis, Fig. S6 and S7) reveals an endothermic event around 302 °C for both **1** and **2**, involving the release of approximately 281.44 (**1**) and 245.4 J $g^{-1}$ (**2**), which is associated with the thermal decomposition of the complex. Given the polymeric nature of the structure and the abrupt profile of the peak, this event is unlikely to correspond to a melting process. Instead, it most likely results from dissociating the metal–ligand framework and subsequent structural collapse. A deviation in the baseline is also observed around 90 °C. Although no mass loss is detected in this region by TGA, this thermal event may reflect a subtle structural relaxation or rearrangement within the crystalline lattice, possibly involving weak non-covalent interactions or minor reorganization of the supramolecular packing. The remarkable thermal stability of these oxamate complexes may be associated with the polymeric nature of **1** and **2** and the lack of solvent molecules in their molecular structures, as is normally observed in oxamate complexes.[43,44]

The SCXRD data reveal that **1** and **2** are anionic coordination polymers and isostructural (corroborated by the experimental and simulated PXRD in Fig. S8 and S9) that crystallize in the non-centrosymmetric hexagonal space group $P6_522$ (Table S1). The polymer's counterion is an *n*-tetrabutylammonium cation with no crystallization solvent molecules. The CIF files were deposited at the Cambridge Crystallographic Data Center (CCDC) under the numbers 2455991 (**1**) and 2455992 (**2**). Since compounds **1** and **2** are isostructural, showing only minor differences in bond lengths and angles, the crystal description is detailed for compound **1**, with differences relative to compound **2** highlighted when relevant.

Coordination polymer **1** comprises a $Tb^{3+}$ ion coordinated to four oxamate groups in the $TbO_8$ coordination sphere (Fig. 1(a) and (b)). A similar coordination environment is observed for **2**, where the metal ion is $Gd^{3+}$. In both compounds, each oxamate group is from a different $H_2$edpba$^{2-}$ ligand, which bridges to metal ions. The coordination polymer

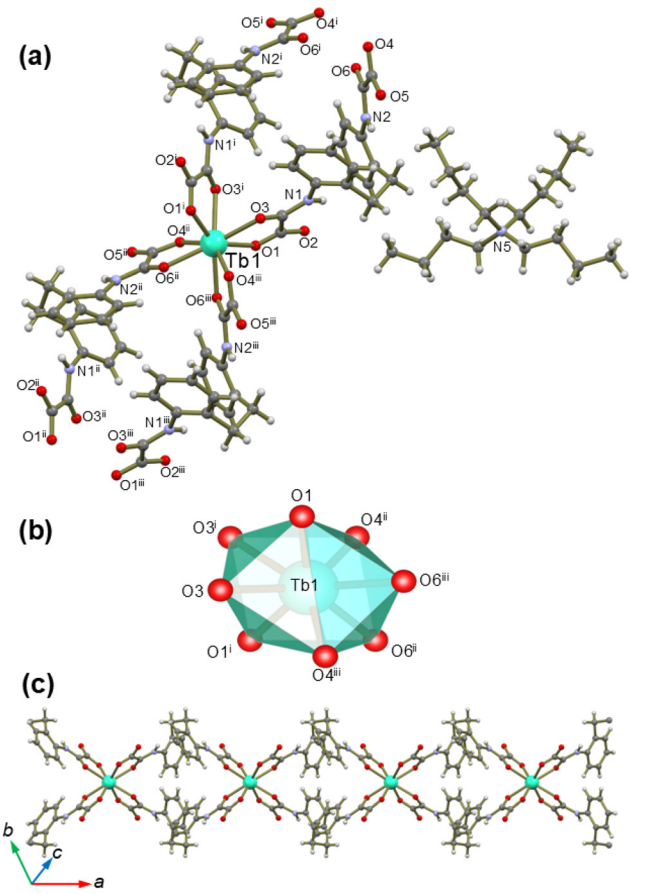


**Fig. 1** (a) Crystal structure of **1** showcasing the four $H_2$edpba$^{2-}$ ligands coordinated to the terbium atom. Terbium, nitrogen, and oxygen atoms are labelled accordingly. Carbon (in grey) and hydrogen atoms (in white) are not labelled for clarity. (b) Coordination polyhedron around the terbium atom. Symmetry codes: i = –1 + *x* – *y*, 2 – *y*, 1 – *z*, ii = *x* – *y*, 2 – *y*, 1 – *z*, iii = –1 + *x*, *y*, *z*. (c) Coordination polymer of **1** growing parallel to the crystallographic *a* axis.

exhibits a ribbon chain-like structure, yielding a metallacycle in which the metal atoms link the rings formed by the ligands, as illustrated in Fig. 1(c).

The terbium(III) ions in **1** coordinate with the oxamate by the amide oxygen atom and one of the carboxylate oxygen atoms in bidentate form, forming four five-membered rings fused on the corner occupied by the metal atom. All oxygen-metal distances are in the range of *ca.* 2.30–2.45 Å for **1** and 2.32–2.48 Å for **2**, which is the characteristic of lanthanide-to-oxygen atom bond length,[37,38] leading to the metal atom being in a distorted square antiprism coordination geometry. Each oxamate group fills two positions on the same side of the square antiprism polyhedron (Fig. 1(b)). The coordination geometry was tested once more using SHAPE software[30] (Table S2), based on the atomic positions of the atoms extracted from the crystal structure, which is close to the square antiprism geometry (SAPR-8 – $D_{4d}$ point group). The selected bond lengths and angles for all metal complexes are found in Table S3. The closest intermetallic distance inside the polymer is equal to 11.61340(10) Å for Tb1···Tb1$^{iv}$ (iv = 1 + $x$, $y$, $z$) [11.6877(2) Å for Gd1···Gd1$^{iv}$, for **2**], suggesting that metal ions are well isolated in the crystal structure. It is worth remarking that this is the highest intermetallic distance for an Ln···Ln oxamato complex found in the literature.[45]

The $H_2$edpba$^{2-}$ ligand is linked to two metal ions, one in each oxamate group, acting in the μ-κO,O′:κO″,O‴ coordination mode. The oxamate groups are not coplanar to the phenyl rings for the polymer to reach the chain-like structure. The angles between the mean plane of the oxamate groups formed by the N1O1O2O3 and N2O4O5O6 sets of atoms and the aromatic ring linked directly to them are 36.6(7)° and 15.3(3)°, respectively. Additionally, the ethane carbon chain linking the phenyl rings is found in the *gauche* conformation, and the torsion angle around this C–C bond is 63.8(4)°, which is very close to the perfect torsion angle for this conformation.

Crystal packing is formed by polymers packed in supramolecular planes along the crystallographic *ab* plane, and it alternates with *n*-butylammonium cation layers (Fig. 2). The layers are packed along the *c* crystallographic axis, and the polymers grow along the crystallographic *a*, *b*, or *a* + *b* axis. In each separate polymer layer, they are all parallel and grow in a single direction. In the next layer, they grow at 60° to the previous one, forming a three-layer alternating orientation packing similar to the ABC close packing arrangement. At the same layer, the shortest intermetallic distance is also equal to 11.61340(10) Å for Tb1···Tb1$^{v}$ in **1** and 11.6877(2) Å, for Gd1···Gd1$^{v}$ in **2** [v = $x$, 1 + $y$, $z$]. Inside this layer, the neighbour coordination polymers are found interacting *via* C–H···O weak hydrogen bonds, involving the aromatic hydrogen atoms and the non-coordinated carboxylate oxygen atom. Only van der Waals interactions between the various aliphatic carbon chains are found for the cation layers. Finally, between the polymers and the *n*-butylammonium layers, van der Waals interactions between the phenyl rings of the ligands and the aliphatic carbon chains of the *n*-butylammonium ions are present. Along this direction, the closest metal–metal distance is equal to 11.0141(19) Å for Tb1···Tb1$^{vi}$ (vi = –1 + $y$, –$x$ + $y$, 1/6 + $z$) [11.1156(1) Å for Tb1···Tb1$^{vi}$ in **2**].

The direct current (dc) magnetic properties of **1** and **2** were investigated in the crystalline powder samples of **1** and **2** using $\chi_M T$ *vs.* $T$ and $M$ *vs.* $HT^{-1}$ plots [$\chi_M$, $M$ and $H$ are the molar magnetic susceptibility, molar magnetization and applied dc

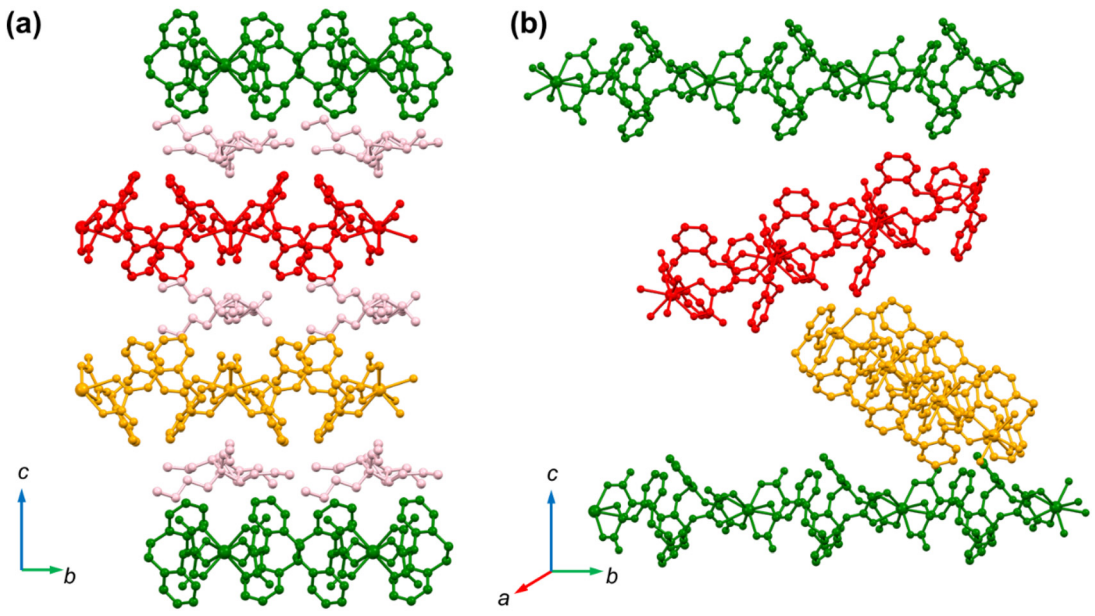


**Fig. 2** (a) Crystal packing of **1** along the crystallographic *a* axis, showcasing the alternating pattern of polymers and *n*-butylammonium layers. The *n*-butylammonium cations are coloured pink. The polymers are green, orange, or red depending on the growing direction. The polymers growing along the *b* axis are depicted in green, those growing along the *a* axis are in red, and those growing along the *a* + *b* direction are in orange. (b) Different growing directions of the polymers in each layer of the crystal packing.

 

magnetic field, respectively], as shown in Fig. 3. At 300 K, the experimental $\chi_M T$ value for **1** is 11.49 $cm^3$ K $mol^{-1}$ (**1**) Fig. 3(a). This is very close to the theoretical value of 11.82 $cm^3$ K $mol^{-1}$ expected for a free single terbium(III) ion [considering $L$ = 3; $S$ = 3; $J$ = 6, and $g_J$ = 3/2, $^7F_6$]. For **1**, the $\chi_M T$ product gradually decreases upon cooling, reaching 11.14 $cm^3$ K $mol^{-1}$ at 100 K, and a minimum at 10 K ($\chi_M T$ = 10.30 $cm^3$ K $mol^{-1}$). The decrease in $\chi_M T$ product **1** is mainly attributed to the depopulation of higher energy $m_J$ states (Stark levels) induced by the ligand field effect, which is very pronounced in lanthanide complexes.[4] The $\chi_M T$ product at 10 K typically falls within the 8.9–9.5 $cm^3$ K $mol^{-1}$ range of similar compounds.[45] Therefore, compound **1** does not exhibit a pronounced decrease in the $\chi_M T$ product as observed in other previously reported terbium (III)-oxamate complexes.[46,47] Below 10 K, a slight increase in the $\chi_M T$ product is verified, reaching 10.38 $cm^3$ K $mol^{-1}$ at 2.4 K. This temperature-dependent increase is associated with dipolar ferromagnetic interactions, which are commonly found in lanthanide compounds with high spin values.[48] The reduced magnetization curves measured at 2 K for **1** exhibit a significant increase of up to approximately 10 kOe in magnetization, after which it begins to saturate, reaching 4.74 $N_A\mu_B$ at 70 kOe (inset of Fig. 3(a)). As the temperature increases, this saturation effect becomes progressively less pronounced. However, the magnetization values at temperatures ranging from 2 to 10 K under a 70 kOe field remain relatively close (4.74 $N_A\mu_B$ at 2 K and 4.55 $N_A\mu_B$ at 10 K).

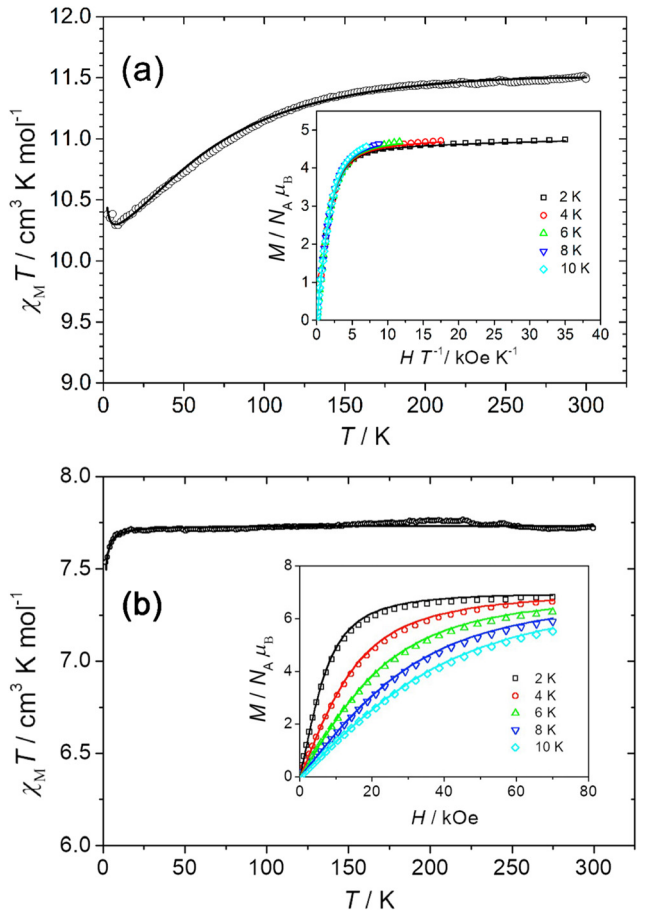


**Fig. 3** Temperature dependence of the $\chi_M T$ product for **1** (a) and **2** (b) [H = 200 Oe]. (a) Insets: *M versus* $HT^{-1}$ curves for **1** and (b) *M versus H* curves for **2**, respectively, at 2, 4, 6, 8, and 10 K. Solid lines represent the simulations of the experimental data, as described in the text.

Notably, the reduced magnetization curves for **1** (inset of Fig. 3) do not show a clear overlap among the curves, indicating significant anisotropy.

To better understand these observations, simulations of the $\chi_M T$ *vs.* $T$ and $M$ *vs.* $H$ curves were performed for **1**. For this purpose, the following Hamiltonian (eqn (1)) was used:

$$\boldsymbol{H} = \lambda(\boldsymbol{L}\cdot\boldsymbol{S}) + \Delta[\boldsymbol{L}_z{}^2 - \boldsymbol{L}^2] + (-\kappa\boldsymbol{L} + 2\boldsymbol{S})\mu_B\boldsymbol{B}, \quad (1)$$

where $\lambda$ is the spin–orbit splitting parameter within the ground electronic term; $\Delta$ represents the energy gap between the $M_L$ values; $\kappa$ is the orbital reduction parameter (fixed at $\kappa$ = 1); $\mu_B$ is the Bohr magneton; and $\boldsymbol{L}$, $\boldsymbol{S}$, and $\boldsymbol{B}$ represent the angular momentum operator, spin operator, and magnetic field vector, respectively. Using the Hamiltonian described above, which is implemented in the PHI software,[49] a theoretical curve shows excellent agreement with the experimental data for **1** ($R$ = 0.676, where $R = \left[\sum_{i=1}^{\text{points}} (M_{\text{exp}} - M_{\text{calc}})^2\right]\left[\sum_{i=1}^{\text{points}} (\chi_{\text{exp}} - \chi_{\text{calc}})^2\right]$, where $M_{\text{exp}}$ and $M_{\text{calc}}$ denote the experimental and calculated magnetization values for the $M$ *vs.* $H$ curves, respectively, while the $\chi_{\text{exp}}$ and $\chi_{\text{calc}}$ are the experimental and calculated susceptibility for the $\chi_M T$ *vs.* $T$ curve, respectively). To reproduce an increase in the $\chi_M T$ *vs.* $T$ curve at low temperatures, a $zJ$ component was introduced in that model. The values obtained ($\lambda$ = −225.47 $cm^{-1}$, $\Delta$ = −88.93 $cm^{-1}$, and $zJ$ = +1.67 × $10^{-3}$ $cm^{-1}$) from the simulation for spin–orbit splitting parameter, axial distortion, and mean-field model for coupling for **1**, respectively, exhibit strong consistency with previously reported values for compounds containing $Tb^{3+}$ ions.[46,47,50] Adjustments were performed considering positive axial distortion parameters ($\Delta$). However, poor agreement with the experimental values was observed, particularly at low temperatures, where the experimental $\chi_M T$ product exhibits a much less pronounced decrease than the simulated curve with positive axial distortion values. The negative axial distortion values indicate that states with higher $m_J$ values have low energy, with the ground state corresponding to $m_J$ = ±6. The relatively high value of axial distortion parameter $\Delta$ suggests a strong splitting of the $m_J$ states, indicating the presence of axial-type anisotropy.[48] The presence of magnetic interactions in compounds containing lanthanide ions at low temperatures is not uncommon, even though the magnetic orbitals of these compounds have a significant contribution from the f orbitals, which are more internally localized.[51–54] These interactions, especially when the metal atoms are spaced apart, exhibit a dipolar nature since the internal characteristics of the 4f orbitals greatly hinder exchange and superexchange interactions. **1** is composed of terbium(III) dimers isolated by tetrabutyl-

ammonium cations. The shortest distance between the $Tb^{3+}$ ions is 11.61 Å, thus leaving only the possibility of dipole–dipole interactions, which are present in compounds containing paramagnetic ions with a high spin value, which in the case of $Tb^{3+}$ ions is $S = 6/2$.[48]

At 300 K, the experimental $\chi_M T$ value for **2** is 7.71 $cm^3$ K $mol^{-1}$ (Fig. 3(b)), which is very close to the theoretical value of 7.88 $cm^3$ K $mol^{-1}$ expected for a gadolinium(III) ion [considering $L = 0$; $S = 7/2$; $J = 7/2$, and $g_J = 2$, $^8S_{7/2}$]. Values of $\chi_M T$ obey the Curie Law in a wide range of temperatures and start to deviate from linearity at 16 K, reaching their minimum at 1.88 K ($\chi_M T$ = 7.54 $cm^3$ K $mol^{-1}$), which depicts a very weak antiferromagnetic behavior.

The magnetization *versus* field curve for compound **2**, measured at 2 K, exhibits a sharp increase of up to approximately 8 kOe (4.45 $N_A\mu_B$) in magnetization, after which the rate of increase slows down until around 40 kOe (6.65 $N_A\mu_B$). Beyond this field, the magnetization tends toward saturation, reaching 6.82 $N_A\mu_B$ at 70 kOe. As expected, as the temperature increases, the saturation effect becomes much less pronounced, and at 10 K, the magnetization curve appears almost linear, up to approximately 20 kOe. The reduced magnetization curve for compound **2** (Fig. S10) displays a complete overlap, which is consistent with the expected behavior for a gadolinium(III) complex due to the lack of magnetic anisotropy.

To better understand these results, a model considering isotropic $Gd^{3+}$ ions, including a $zJ$ component to account for intermolecular coupling (molecular field approximation model), was employed to simultaneously fit the $\chi_M T$ *vs.* $T$ and $M$ *vs.* $H$ curves (Fig. 3b).[55] This model was implemented in the PHI software using a basic isotropic Heisenberg Hamiltonian.[49] Using this model, a theoretical curve shows excellent agreement with the experimental data ($R$ = 1.498, where $R$ has the same meaning as that described for compound **1**). The best-fit parameters obtained for **2** were $g$ = 1.981 ± 0.000 and $zJ$ = −0.002 ± 0.000 $cm^{-1}$. The small value of $zJ$ indicates a very weak antiferromagnetic interaction, as the shortest distance between two $Gd^{3+}$ ions is 11.6877(2) Å, which is likely of dipolar origin, similar to that observed in compound **1**. Due to the large spin value of the $Gd^{3+}$ ions, it is expected that the presence of dipolar interactions will be observed in a more pronounced way in **2** compared to **1**. These fitting parameters agree with those found for a recently oxamate complex $\{Gd(phox)_3(DMSO)_2\}_n \cdot nH_2O$ (phox = *N*-(phenyl)oxamate), reported previously ($g$ = 1.97 ± 0.000 and $zJ$ = −0.002 ± 0.000 $cm^{-1}$).[50]

The dynamic behavior of samples **1** and **2** was investigated under alternating current (ac) in frequencies ranging from 10 Hz to 10 kHz within a field ranging from 0.0 to 5.0 kOe. Fig. 4 shows the dependence of the real ($\chi'$) and imaginary ($\chi''$) components for terbium(III)-based compounds under a 1.0 kOe field in the 2–14 K range (see Fig. 4(a)). The Cole–Cole plots and frequency-dependent $\chi'$ and $\chi''$ measurements under the applied dc fields of $H$ = 0.0, 0.5, 2.5 and 5.0 kOe are shown in Fig. S11–S14 for **1**. The Cole–Cole plots display semicircles and

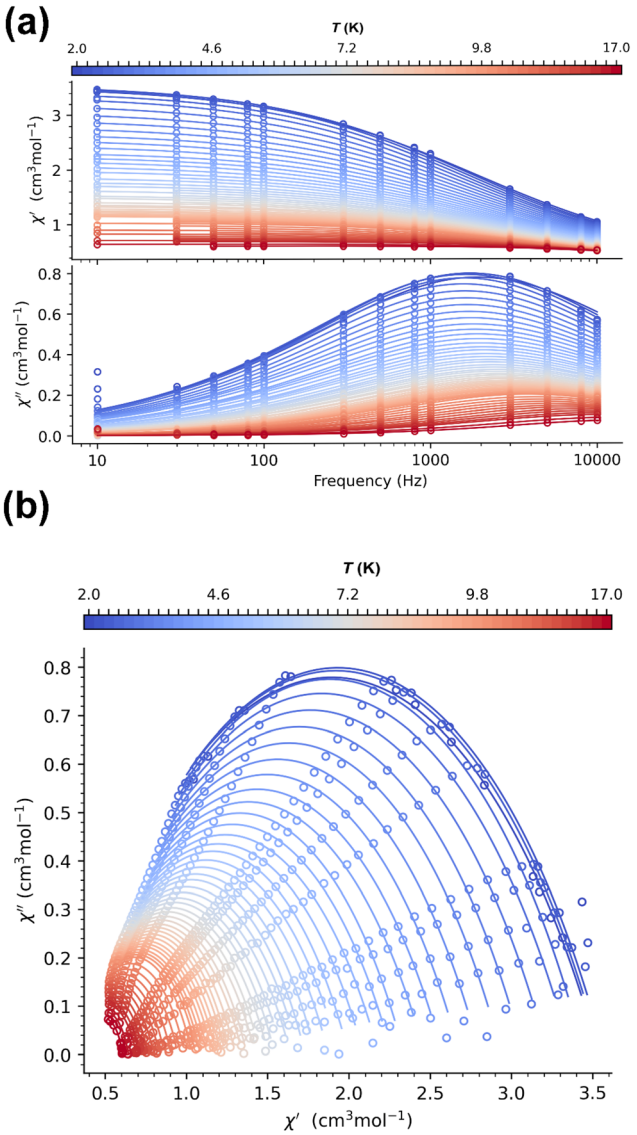


**Fig. 4** (a) Real ($\chi'$) and imaginary ($\chi''$) components of the magnetic susceptibility of compound **1** in the temperature range of 2.0 to 17.0 K at 1.0 kOe and the frequency range of 10 Hz–10 kHz. (b) Cole–Cole plot for **1**. The solid lines in the parts represent the best-fit curves using the parameters from the generalized Debye model.[56]

symmetrical shapes, which are attributed to the slow magnetization relaxation process, within an $\alpha$ range of 0.25–0.44, a moderate distribution of relaxation times. **1** is an SIM, as in the absence of an applied magnetic field (Fig. S11), it shows significant values for the imaginary component of magnetic susceptibility. However, the data at 1.0 kOe were displayed in this study because they present a better resolution. The Cole–Cole plots at several temperatures are illustrated in Fig. 4(b).

Fig. 5(a) displays the frequency dependence of the real ($\chi'$) and imaginary ($\chi''$) components for **2**, which is measured under a dc field of 5.0 kOe between 2.0 and 14.0 K. In the temperature range of 2.0–4.0 K, the system exhibits anomalous temperature dependence: the $\chi''$ peak maximum shifts to lower frequencies, while its amplitude increases as the temperature

 

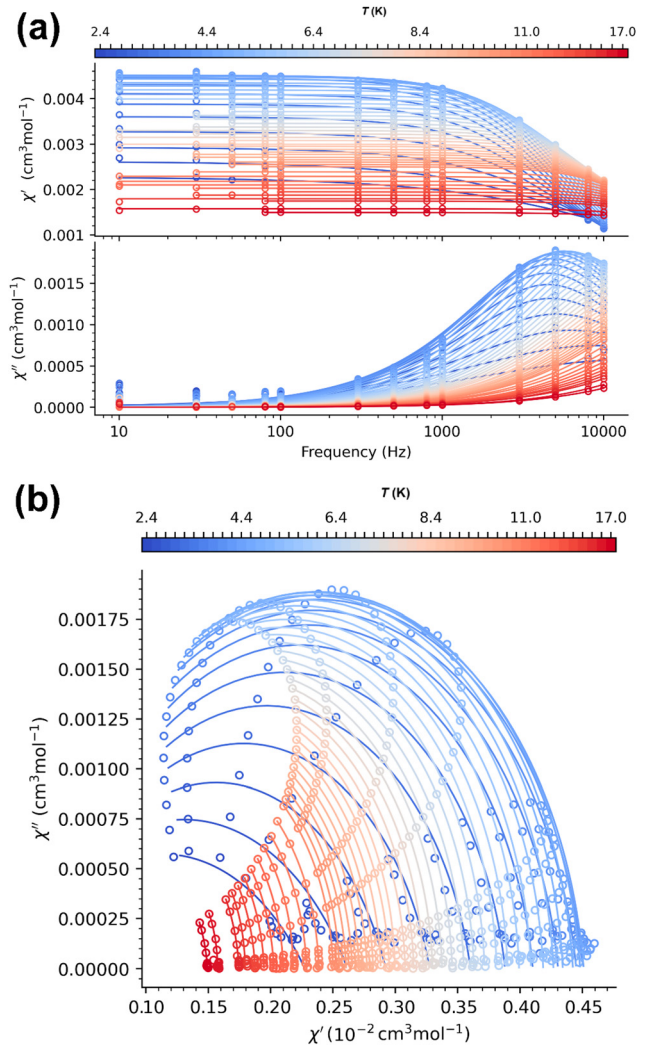


**Fig. 5** (a) Real ($\chi'$) and imaginary ($\chi''$) components of the magnetic susceptibility of compound **2** in the temperature range of 2.0 to 17.0 K at 5.0 kOe and the frequency range of 10 Hz–10 kHz. (b) Cole–Cole plot for **2**. The solid lines in the parts represent the best-fit curves using the parameters from the generalized Debye model.[56]

increases. Above this range, the behavior reverts to the conventional trend: the $\chi''$ peak shifts to higher frequencies, while its amplitude decreases with further warming, as shown in Fig. 5(a). The Cole–Cole plots and frequency-dependent $\chi'$ and $\chi''$ measurements under applied dc fields of $H$ = 0.5, 1.0 and 2.5 kOe are shown in Fig. S15–S17 for **2**. The Cole–Cole plots of **2** measured under a dc field of 5 kOe at several temperatures are displayed in Fig. 5(b). The Cole–Cole plots are characterized by semicircular arcs but with anomalous peak shifts, with the semicircles moving rightward between 2.0–4.0 K and leftward with a further increase in temperature. This temperature dependence is also observed clearly in the ac susceptibility data of the terbium(III) complex under dc fields of 2.5 and 5.0 kOe. For the gadolinium(III) complex, similar complex behavior occurs under dc fields of 1.0, 2.5, and 5.0 kOe. This behavior suggests distinct mechanisms governing the slow magnetization relaxation process of these complexes at different temperature ranges.

The frequency-dependent $\chi'$ and $\chi''$ data, measured at different temperatures for both **1** and **2** complexes, were fitted using the generalized Debye model[56] *via* the CCFIT software,[57] revealing the temperature-dependent behavior of the relaxation time. These data, obtained under various applied dc fields, were used to construct the Arrhenius plots shown in Fig. 6 and 7 for the terbium(III) and gadolinium(III) complexes, respectively. The parameters provided by the fittings are presented in Tables S4–S8 (for **1**) and Tables S9–S12 (for **2**) in the SI. The Arrhenius plots of **1** were analyzed by considering eqn (2):

$$\tau^{-1}(T) = CT^{n} + \tau_0^{-1} \exp\left(\frac{-U_{\text{eff}}}{k_{\text{B}}T}\right). \quad (2)$$

The first term represents the Raman process, while the second represents the Orbach process, and fitting the Arrhenius plots using eqn (2) yielded values for $C$, $\tau_0$, and the effective energy barrier ($U_{\text{eff}}$) shown in Table 1. To obtain the $n$ values from fitting the Arrhenius plots, we employed the following procedure: first, we attempted to fit the data with the exponent $n$ fixed to 7.[58,59] Then, for data obtained under a dc field where this approach failed, we allowed $n$ to vary as a free parameter.

The fitting process for data obtained at $H_{\text{dc}}$ = 0 kOe did not produce reasonable $U_{\text{eff}}$ values; thus, only the Raman process was considered, resulting in $n$ = 1.16, which is close to the exponent expected for the direct process.[4]

For an applied dc field of $H_{\text{dc}}$ = 0.5 kOe, the data were well described by the Raman process ($n$ = 7) combined with the Orbach mechanism, yielding a small $U_{\text{eff}}$ value. When the dc field increased to 1.0 kOe, $U_{\text{eff}}$ increased further (see Table 1). For fields of 2.5 and 5.0 kOe, the Arrhenius plots exhibit saturation at low temperatures, with a maximum that can be inferred for the 2.5 kOe case. The saturation is associated with

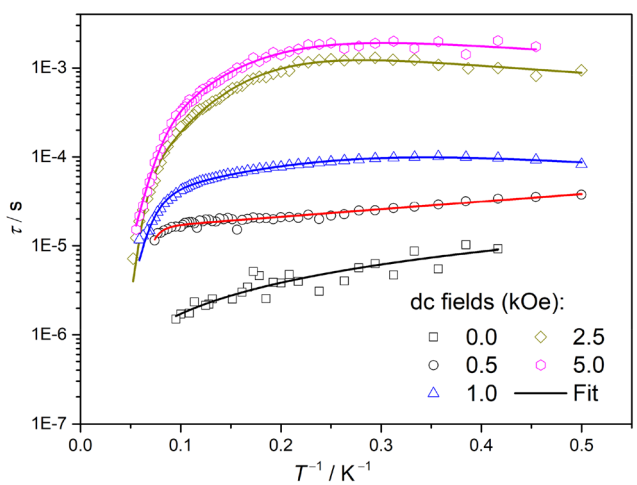


**Fig. 6** Arrhenius plot ($\ln\tau$ *versus* $T^{-1}$) under various applied dc fields ($H_{\text{dc}}$ = 0.0, 0.5, 1.0, 2.5, and 5.0 kOe) for **1**. The solid line represents the best-fit curves of the experimental data, considering the processes discussed in the text.

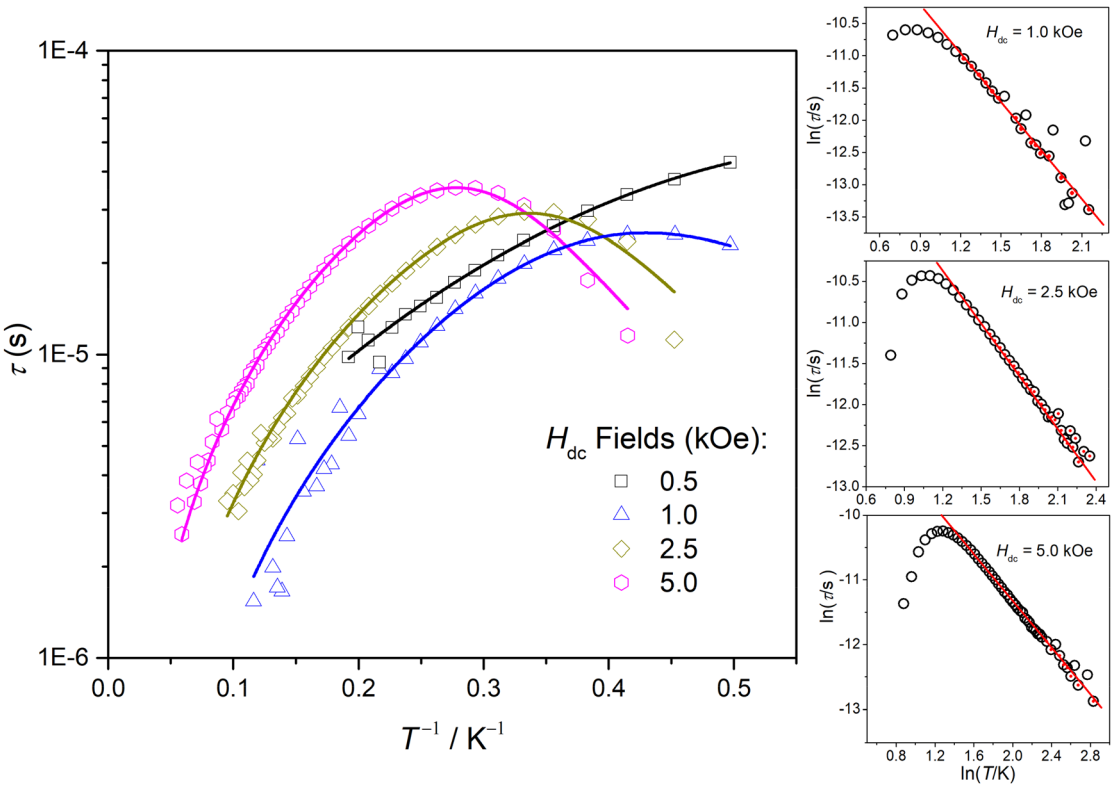


**Fig. 7** Temperature dependence of the relaxation time for **2**. Left: Arrhenius plots (ln $\tau$ *versus* $T^{-1}$) under various applied dc fields ($H_{dc}$ = 0.5, 1.0, 2.5, and 5.0 kOe) for **2**. The solid line represents the best-fit curves of the experimental data, considering the processes discussed in the text. Right: ln $\tau$ *versus* ln $T$ for different applied dc fields ($H$ = 1.0, 2.5, and 5.0 kOe). Filled data points were used in linear regression according to the equation $\ln\tau = -\ln(C) - n\ln(T)$.

**Table 1** Dynamic magnetic parameters of **1** and **2**

| Compound | Parameter/$H$ (kOe) | 0 | 0.5 | 1.0 | 2.5 | 5.0 |
|---|---|---|---|---|---|---|
| **1** | $C$ ($s^{-1}$ $K^{-n}$) | 40.2(1) × $10^3$ | 4.2(2) × $10^3$ | 3.6(6) × $10^3$ | 9.6(6) × $10^3$ | 0.16(1) |
| | $n$ | 1.16(12) | 7 | 7 | 7 | 2.64(17) |
| | $\tau_0$ (s) | | 1.42(3) × $10^{-5}$ | 2.51(11) × $10^{-5}$ | 4.4(5) × $10^{-5}$ | 3.8(21) × $10^{-8}$ |
| | $U_{eff}/k_B$ (K) | | 1.98(7) | 7.76(21) | 18.6(7) | 114(70) |
| | $F$ ($K$ $s^{-1}$) | | | 4.8(7) × $10^{-5}$ | 4.2(1) × $10^{-4}$ | 7.9(4) × $10^{-4}$ |
| **2** | $C$ ($s^{-1}$ $K^{-n}$) | | 7.4(4) × $10^3$ | 2.1(7) × $10^3$ | 2.7(4) × $10^3$ | 2.2(1) × $10^3$ |
| | $n$ | | 1.6(1) | 2.6(2) | 2.1(1) | 2.0(1) |
| | $F$ ($K^b$ $s^{-1}$) | | 7(2) × $10^6$ | 3.9(12) × $10^5$ | 1.7(3) × $10^6$ | 2.0(3) × $10^7$ |
| | $b$ | | 2.5(2) | 2.6(1) | 7.2(3) | 4.96(2) |

the QTM relaxation process. However, as no QTM relaxation process was observed at a zero applied dc field, it was neglected in the analysis of the Arrhenius plots for all applied dc field values. The maximum in the Arrhenius plots observed at low temperatures suggests the occurrence of reciprocating thermal behavior (RTB).[58–60] RTB, a second solution of the phonon-bottleneck effect, exhibits a temperature dependence of $\tau^{-1} \propto T^{-b}$ ($b > 0$). Consequently, the Arrhenius plots were fitted using eqn (3):

$$\tau^{-1}(T) = CT^n + {\tau_0}^{-1}\exp\left(\frac{-U_{eff}}{k_B T}\right) + FT^{-1}. \quad (3)$$

For complex **1**, exponent $b$ was fixed at 1 to prevent overparametrization. The $C$, $n$, and $F$ values obtained for applied dc fields of 1.0, 2.5, and 5.0 kOe are shown in Table 1. For an applied field of 5.0 kOe, the value obtained for the exponent of the Raman process is close to 2.0, suggesting the occurrence of the normal phonon-bottleneck with a temperature dependence of $\tau^{-1} \propto T^2$ in addition to RTB.[4]

The slow magnetic relaxation mechanism of **1** is governed by a temperature exponent $\tau^{-1} \sim T^n$ (with $n$ = 1.16) under zero applied dc field and Raman and Orbach processes at 0.5 kOe (eqn (2)). At the same time, at 1.0, 2.5 and 5.0 kOe (eqn (3)), the Raman, Orbach and reciprocating thermal behavior take place.

 

For **1**, the reciprocating thermal behavior occurs within the magnetic field and temperature range (low temperature), where anomalous temperature behavior is exhibited in both the imaginary ($\chi''$) component of magnetic susceptibility and the Cole–Cole plots. This anomalous temperature behavior is also observed for **2**, which has an isotropic ground state with near-zero magnetic anisotropy, preventing the Orbach process. The Arrhenius plot of **2** showed a decrease in relaxation time as the temperature decreased within the same range, where anomalous behavior was observed in the Cole–Cole plots. This suggests that this effect is associated with RTB (see Fig. 7). Consequently, the $\tau$ *vs.* $T^{-1}$ plots for **2** were fitted using eqn (4).

$$\tau^{-1}(T) = CT^{n} + FT^{-b}. \quad (4)$$

In this analysis, the exponent of the RTB process was considered with a free exponent ($b$).

For a 0.5 kOe applied field, the anomalous temperature behavior was not observed. These data were fitted using only the $CT^n$ process from eqn (4) over the entire temperature range. The resulting best-fit parameters are shown in Table 1. For other applied dc fields ($H_{dc}$ = 1.0, 2.5, and 5.0 kOe), the data were fitted considering both processes in eqn (4). For these dc field values, we used the following procedure to improve the accuracy of the exponent and coefficient values obtained from the fit of the relaxation time to temperature. First, we performed a linear fit on the ln $\tau$ *vs.* ln $T$ plots in the region dominated by $CT^n$ relaxation, thereby determining the coefficient $C$ and the exponent $n$ (right side of Fig. 7). With these values fixed in eqn (4), we then fitted the Arrhenius plots by considering $F$ and $b$ as free parameters (left side of Fig. 7). The $C$, $n$, $F$, and $b$ values obtained for applied dc fields of 0.5, 1.0, 2.5, and 5.0 kOe are shown in Table 1, respectively. For data measured at 1.0, 2.5, and 5.0 kOe, the values obtained for the exponent of the Raman process are in the range of 1.6–2.6, which is in the range of values observed for the bottleneck effect.[58] The exponent values of the RTB were found to be in the range of 2.6–7.2, which is higher than the values previously observed for other molecular complexes.[45] The RTB is observed as one of two processes occurring within the same temperature range in mononuclear complexes (such as $Co^{2+}$, $Mn^{2+}$, and $Ni^{2+}$) and some complexes containing $Gd^{3+}$, such as Ni–Gd.[61–64] We believe that the high values observed for the RTB exponent in the Gd complex are associated with the clear anomalous behavior observed in its Arrhenius plot and Cole–Cole plots (including the frequency dependence of $\chi''$ at low temperature), along with the fact that only one process occurs in this complex for measurements performed at fields of 2.5 and 5.0 kOe.

The values of the Raman coefficient (Table 1) of **1** at 0 and 5.0 kOe are below the expected ones for a non-Kramer ion [$n$ = 7], which suggests the presence of both acoustic and optical phonon processes coupled in the compound.[8] It is worth noting that RTB is a non-traditional thermal behavior in SIMs, and to the best of our knowledge, this is the first report of this behavior that explains the slow magnetic relaxation mechanism in a terbium(III) coordination compound.[58,59] This behavior may have been overlooked, and more examples should be prepared to shed light on the SMR mechanism in Ln-SIMs.[59] Some reports involve complexes with metals from the d-block ($Mn^{2+}$, $Co^{2+}$, $Ni^{2+}$, and $Cu^{2+}$) and 4f block (gadolinium(III), dysprosium(III) and erbium(III)).[58,60,65,66] A recent study describes the observation of RTB phenomena in dysprosium(III) complex $\{[Dy_2(Hpcpa)_3(H_2O)_5]\}_n$ ($H_3$pcpa = *N*-(4-carboxyphenyl)oxamic acid) below 5 K with $H$ = 2.5 kOe.[64] In this latter compound, two $Dy^{3+}$ crystallographically independent ions are octacoordinated, and they exhibit an intermediate between $D_{2d}$ and $D_{4d}$, and $C_{2v}$ symmetries. Considering other examples involving terbium(III) and gadolinium(III) oxamate complexes, the most common mechanism accounting for the SMR phenomena is the phonon bottleneck for $Gd^{3+}$ complexes with $C_{4v}$ and $D_{3h}$ symmetries.[37,45,50,67] In contrast, the Orbach mechanism is described in one example of an octacoordinated complex with $T_d$ symmetry.[47] For terbium(III) oxamate complexes, a combination of Raman and direct, or Raman and QTM mechanisms has been reported for compounds with $D_{3h}$ symmetries.[37] Despite the examples described suggesting that axiality may account for the RTB behavior, more examples are necessary to be synthesized and studied to elucidate this phenomenon better.[48,67]

Beyond its remarkable magnetic behavior, the luminescence properties of **1** were investigated to assess its potential as a luminescent thermometer. The solid-state emission spectra recorded at room temperature (298 K) and 77 K (Fig. 8) reveal the efficient sensitization of $Tb^{3+}$ emissions by oxamate ligands. The excitation spectra ($\lambda_{em}$ = 546 nm) display narrow, low-intensity $Tb^{3+}$ 4f–4f absorptions (350–500 nm), along with a two-component broad band (230–340 nm) corresponding to ligand-centered absorptions ($\pi^* \leftarrow \pi$ and/or $\pi^* \leftarrow \sigma$ tran-

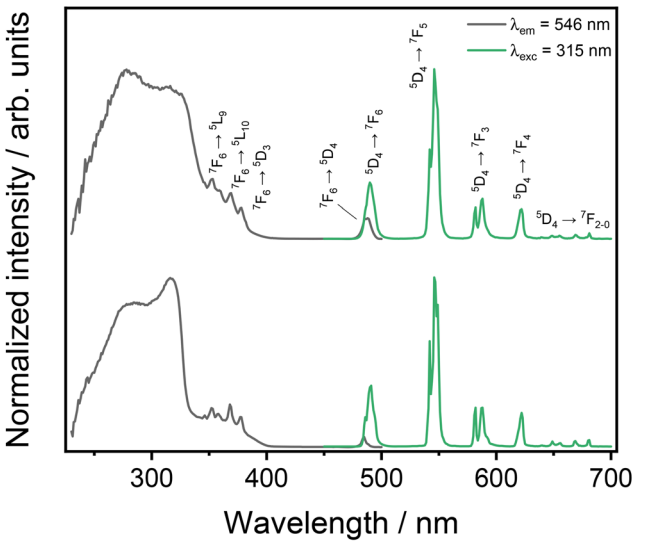


**Fig. 8** Excitation ($\lambda_{em}$ = 546 nm, black line) and emission ($\lambda_{exc}$ = 315 nm, green line) spectra of compound **1** recorded at room temperature, 298 K (top) and 77 K (bottom).

sitions)[37] and $4f^8 \rightarrow 4f^7 5d^1$ absorption of $Tb^{3+}$ ion.[68] Upon UV excitation ($\lambda_{exc}$ = 315 nm, Fig. 8) or direct excitation into the $^5D_4$ level ($\lambda_{exc}$ = 486 nm, Fig. S18), the emission spectra exhibit the characteristic $Tb^{3+}$ emissions comprising the $^5D_4 \rightarrow {}^7F_J$ ($J$ = 6–0) transitions. The absence of detectable luminescence from the organic ligand confirms an energy transfer to the $Tb^{3+}$ excited states, which is further supported by the overall quantum yield measurement ($\phi$ = 10%). This value is comparable to that reported for the europium-based oxamate complex $\{Eu(Hmpa)_3(DMSO)_2\}_n$ [Hmpa = *N*-(4-methylphenyl)oxamate] ($\phi$ = 11%)[69] and significantly higher than that of the oxamate-based isoreticular metal–organic framework-3 (IRMOF-3) ($\phi$ < 1%).[70]

To gain further insight into photophysical behavior, isostructural $Gd^{3+}$ coordination polymer **2** was synthesized, enabling the detection of ligand-centered emission and excitation bands (Fig. S19). The time-resolved phosphorescence spectra recorded at 77 K revealed a triplet-state ($T_1$) energy of around 22 960 $cm^{-1}$. Consequently, the energy gap between the $T_1$ level and the main accepting state of $Tb^{3+}$ ($^5D_4$, 20 500 $cm^{-1}$) in **1** is approximately 2460 $cm^{-1}$, a value well-suited for efficient $Tb^{3+}$ sensitization.[71] Moreover, the arithmetic subtraction of the diffuse reflectance spectra of **1** and its $Gd^{3+}$ analogue unveils a broad band in the 23 200–27 800 $cm^{-1}$ range (Fig. S20), which is tentatively assigned to a metal-to-ligand charge transfer (MLCT) state.[72–74] The presence of this MLCT state suggests an additional non-radiative relaxation pathway, which is potentially thermally activated. These findings indicate that the electronic structure of compound **1** provides attractive pathways for temperature determination.

To explore its viability as a luminescent thermometer, we examined the temperature-dependent optical properties between 77 and 473 K, focusing on both relative emission intensities and luminescence lifetimes (Fig. 9 and S21). The emission spectra ($\lambda_{exc}$ = 315 and 486 nm, Fig. S18) exhibited a uniform decrease in all $Tb^{3+}$ emission bands as the temperature increased, which is consistent with the thermal quenching of transitions originating from the same emitting state ($^5D_4$).[72,75] This homogeneous thermal dependence across the emission bands precludes the establishment of robust correlations based on the intensity ratio between the two emissions, thereby limiting the applicability of luminescence intensities as reliable thermometric parameters.

In contrast, the emission decay profiles of the $^5D_4$ level monitoring the transition $^5D_4 \rightarrow {}^7F_5$ (546 nm) demonstrated a thermometric potential of **1** (Fig. 9(a) and (b)). Regardless of the excitation wavelength, the $^5D_4$ lifetimes obtained from single-exponential fits of the experimental decays decreased by only ~4% between 77 and 323 K. However, further temperature increases significantly changed the excited-state kinetics, leading to a 90% reduction of emission lifetime in the 323–473 K range (Fig. 9(a) and (b), and Table S13). This behavior is typically found in correlated lanthanide-based luminescent systems[76–78] and stems from a thermal quenching process involving $Tb^{3+}$ and ligand excited states.

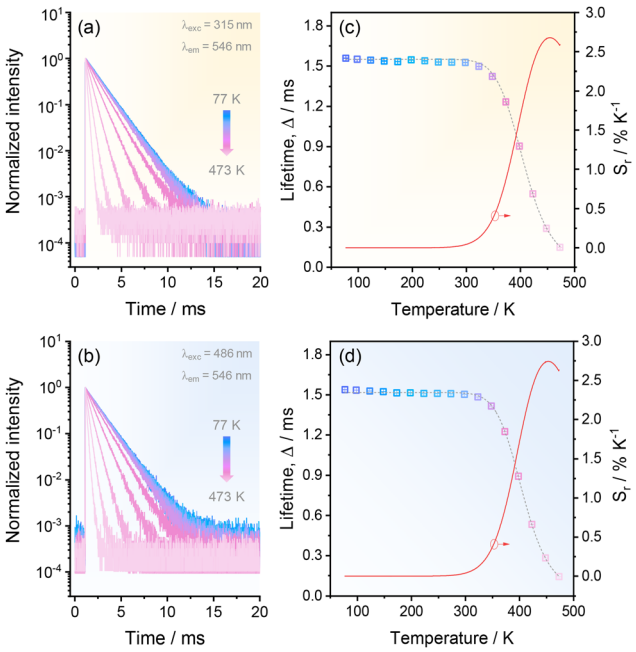


**Fig. 9** Temperature-dependent emission decay curves of **1** monitoring the $^5D_4 \rightarrow {}^7F_5$ $Tb^{3+}$ transition ($\lambda_{em}$ = 546 nm) under excitation at (a) 315 nm (ligand absorption) and (b) 486 nm ($^5D_4 \leftarrow {}^7F_6$ $Tb^{3+}$ absorption). (c) and (d) Thermal dependence of the lifetime (thermometric parameter, Δ) and the relative thermal sensitivity ($S_r$, red line) under excitation at (c) 315 nm and (d) 486 nm; the gray dotted lines correspond to modelled data using eqn (4) ($r^2$ > 0.999).

We then used the $^5D_4$ lifetime as the thermometric parameter, Δ, to quantify the thermal sensing ability of **1**. The temperature dependence of Δ between 77 and 473 K was described in terms of the classical Mott–Seitz model[79,80] for a single non-radiative recombination channel according to eqn (5):

$$\Delta(T) = \frac{\tau_0}{1 + \alpha \exp\left(\frac{-\Delta E}{k_B T}\right)}, \quad (5)$$

where $\tau_0$ is the lifetime at $T$ = 0 K, $\alpha$ is the ratio between non-radiative and radiative rates, and $\Delta E$ is the activation energy for the non-radiative channel. The final $\Delta$ *vs.* temperature calibration curves showed good correlations with the proposed model ($r^2$ > 0.999, Fig. 9(c) and (d)), yielding $\tau_0$ = 1.550 ± 0.001 ms, $\alpha$ = (5.8 ± 1.9) × $10^6$, and $\Delta E$ = 4399 ± 134 $cm^{-1}$ for excitation at 315 nm, and $\tau_0$ = 1.517 ± 0.003 ms, $\alpha$ = (8.8 ± 2.1) × $10^6$, and $\Delta E$ = 4516 ± 97 $cm^{-1}$ for excitation at 486 nm. These results support a non-radiative recombination channel governed by thermally driven depopulation of the $^5D_4$ state *via* back energy transfer (B-ET) to the MLCT state, as the activation energies ($\Delta E$ ~ 4500 $cm^{-1}$) match the energy gap between the bottom of the $^5D_4$ level potential curve (~20 500 $cm^{-1}$) and the crossover point with the MLCT state, which spans from 23 200 to 27 800 $cm^{-1}$. Although a competing pathway involving the $T_1$ level[24] cannot be ruled out, the data suggest that B-ET to the MLCT state is the dominant process.

To quantify the thermometric performance, the relative thermal sensitivity ($S_r$) was calculated as a function of temperature as follows (eqn (6)):[81]

$$S_r(T) = \frac{1}{\Delta}\left|\frac{\partial\Delta}{\partial T}\right| \times 100\%. \quad (6)$$

As expected, $S_r$ exhibited a bell-shaped profile, peaking around 423–473 K (Fig. 9(c) and (d)). The maximum relative sensitivities ($S_m$) were 2.73% ± 0.01% $K^{-1}$ and 2.77% ± 0.03% $K^{-1}$ at 448 K for excitation at 315 and 486 nm, respectively. Contrary to most luminescent thermometers based on lanthanide MOFs and complexes,[19,82,83] **1** exhibits high $S_r$ values above 373 K due to its excellent thermal stability. In addition, emission lifetime as a thermometric parameter offers a significant advantage over single-emission-based luminescent thermometers, as it mitigates issues related to optoelectronic fluctuations of the excitation source and material inhomogeneities.[28,84]

Further insight into thermometer performance was achieved by evaluating the minimum expected statistical temperature uncertainty ($\delta T$) using eqn (7):[81]

$$\delta T = \frac{1}{S_r}\left|\frac{\partial\Delta}{\Delta}\right|, \quad (7)$$

where $\delta\Delta/\Delta$ denotes the relative uncertainty in the determination of $\Delta$, which is obtained from the standard deviations of triplicate measurements. The temperature uncertainties remained below 0.7 K across the entire evaluated temperature range (Fig. S22), indicating that **1** can provide highly precise temperature readouts.

From a practical point of view, the thermometric performance of **1** is evaluated not only in terms of emission lifetime but also in terms of the temperature-dependent excitation spectra. By monitoring the $^5D_4 \rightarrow {}^7F_5$ $Tb^{3+}$ transition at 546 nm, we observe partially reduced intensities of the $^5D_4 \leftarrow {}^7F_6$ transition in the 77–473 K range, in contrast to the significant thermal quenching of the ligand-centered and/or interconfigurational $Tb^{3+}$ excitation bands (Fig. S23(a)). Such an inhomogeneous behavior arises from dissimilar thermal dependences of $Tb^{3+}$ and oxamate ligand excited states and enables the development of an SBR luminescent thermometer.[18,25] In this context, the thermometric parameter (SI) was defined as the integrated intensity ratio between the ligand absorptions ($I_L$, 250–340 nm) and $Tb^{3+}$ excitation band ($I_{Tb}$, 470–500 nm). The temperature dependence of the $\Delta = I_L/I_{Tb}$ ratio displayed a sigmoidal profile (Fig. S23(b)) and followed a phenomenological logistic/sigmoidal function (Table S14). The quantitative description of the thermal dependence of $\Delta$ was based on the calculation of $S_r$ and $\delta T$. The maximum relative thermal sensitivity occurs around 323 K and reaches 1.03% ± 0.01% $K^{-1}$, while temperature uncertainties range from ~0.01 to ~0.18 K between 77 and 473 K (Fig. S23(c)). $S_m$ value is obtained at a lower temperature than lifetime-based thermometry ($S_m$ = 2.7% $K^{-1}$ at 448 K). Therefore, the thermal dependence of the excitation spectra enables widening of the temperature range, in which **1** can provide temperature determinations with relatively high sensitivity. Adopting a figure of merit of $S_r > 1\%\ K^{-1}$,[85] this complex can afford useful temperature sensing in the 273–473 K range considering both thermometry modes.

In general, such findings attest to the high potential of **1** to act as an optical thermal sensor, as shown by a comprehensive comparison between the results of this work and other reported $Tb^{3+}$-based luminescent thermometers (Table S15).

# 4. Conclusions

The synthesis, crystalline structure, and magnetic/luminescent characterization of the air-stable compounds *n*-$Bu_4N[Tb(H_2edpba)_2]$ (**1**) and *n*-$Bu_4N[Gd(H_2edpba)_2]$ (**2**) were carried out. The remarkable thermal stability of **1** and **2**, which remain structurally intact up to ~290 °C (~560 K), demonstrates the robustness of their molecular architecture and highlights their potential for applications in magnetic and photoluminescent devices operating under high-temperature conditions.

Single-crystal X-ray diffraction experiments reveal that compounds **1** and **2** are isostructural, and their crystalline structures consist of a 1D ribbon-like coordination polymer structure, with its unit cell repeating in $[Ln(H_2edpba)_2]_n^-$ anions (Ln = $Tb^{3+}$ or $Gd^{3+}$) and tetrabutylammonium acting as counterions. The terbium(III) and gadolinium(III) ions are surrounded by octacoordinated oxygen atoms, exhibiting local symmetry of a square antiprism coordination sphere geometry with a $D_{4d}$ point group.

Cryomagnetic measurements revealed the presence of dipolar interactions at lower temperatures, resulting in very weak ferromagnetic coupling despite the significant distance between terbium(III) ions in the crystalline structure and displaying the idealized symmetry of $D_{4d}$, which suppresses the unwanted quantum tunneling process, as observed. Dynamic magnetic measurements displayed slow magnetic relaxation behavior without applying an external field, in which **1** represents the first example of a zero-field terbium(III)-oxamato SIM. However, achieving strong axiality to obtain high-performance SIMS with a high energy barrier and high blocking temperatures also involves minimizing transverse anisotropy, dipolar interactions, hyperfine effects, vibronic couplings, and other factors.[86,87] Consequently, dipolar interactions appear to account for a reduction in the SIM performance of **1**, in conjunction with the flexibility of the $H_2edpba^{2-}$ ligand. Previous studies have shown that increasing the structural rigidity of oxamate-based compounds makes them better candidates for quantum technologies as molecular qubits.[50]

Additionally, the SMR phenomena observed in **1** are explained by the Raman mechanism at $H_{dc}$ = 0 kOe, while at $H_{dc}$ = 0.5 kOe, Raman and Orbach mechanisms are observed. In contrast, in higher fields ($H$ = 1.0, 2.5, and 5.0 kOe), Raman, Orbach, and reciprocating thermal behavior mechanisms occur. The RTB is a non-traditional thermal behavior observed

in SIMs and is described for the first time in a terbium(III)-oxamate complex. For compound **2**, dipolar interactions appear to accelerate magnetic relaxation, which is consistent with the complete absence of magnetic relaxation at the zero dc field. In measurements under dc applied fields (0.5, 1.0, 2.5, and 5.0 kOe), an unusual magnetic relaxation process is observed and is associated with the RTB process.

Luminescent experiments confirmed the high-intensity emission of terbium(III) ions, demonstrating that the $H_2edpba^{2-}$ ligand effectively sensitizes lanthanide ions in the solid state. Benefiting from its outstanding thermal stability, **1** exhibited reliable lifetime-based thermometric performance in the 77–473 K range, with maximum relative thermal sensitivities of 2.73% ± 0.01% $K^{-1}$ and 2.77% ± 0.03% $K^{-1}$ at 448 K under ligand ($\lambda_{exc}$ = 315 nm) and direct $Tb^{3+}$ ($\lambda_{exc}$ = 486 nm) excitation, respectively. The results suggest that the back energy transfer from $^5D_4$ $Tb^{3+}$ level to the metal–metal charge transfer state governs excited state dynamics, which is responsible for the drastic decrease in emission lifetime with temperature increasing from 323 K. Complementary, the distinct thermal behavior of the narrow absorptions assigned to $Tb^{3+}$ ($^5D_4 \leftarrow {}^7F_6$, 470–500 nm) and the broad band associated with the oxamate ligand and $4f^8 \rightarrow 4f^85d^1$ transitions (250–340 nm) enabled single-band ratiometric thermometry monitoring the $^5D_4 \rightarrow {}^7F_5$ transition at 546 nm. This additional approach provided sensitive detection (1.03% $K^{-1}$ at 323 K), extending the operational window for high-sensitivity ($S_r$ > 1% $K^{-1}$) optical thermometry to 273–473 K. The system proposed herein points towards designing multifunctional materials that potentially can locally access low temperatures. Further studies of these unusual magnetic relaxation mechanisms (RTB) observed for **1** and **2** could lead to new insights into elucidating intriguing aspects in the SMR of lanthanide complexes.

## Author contributions

All authors have approved the final version of the manuscript. C. R. A. J. and L. M. M. contributed to the reported compounds' complete synthesis and chemical characterizations. W. X. C. O. and C. B. P. have acquired the compounds' crystallographic data and structural description. T. F. R. and P. S. O. P. acquired the data for thermal analysis and provided the corresponding interpretation; P. R. T. R., D. M., F. F., and M. K. have carried out the magnetic measurements; E. F. P. and W. C. N. are responsible for the magnetic treatment of the dc and ac data, respectively. R. V. P. and F. A. S. performed the photophysical studies and interpretation. C. L. M. P. conceived the research idea, guided students, and wrote the paper, with contributions from all the authors.

## Conflicts of interest

The authors declare no conflicts of interest to disclose.

## Data availability

The authors confirm that the data supporting the findings of this study are available within the article and its supplementary information (SI). Supplementary information: crystallographic data, selected bond distances and angles, FT-IR spectra, TG/DTA and DSC curves, experimental and simulated PXRD data, continuous shape measurements analysis, magnetic ac curves, and photophysical data. See DOI: **https://doi.org/10.1039/d5qi01603g**.

Raw data can be made available from the corresponding author upon request.

CCDC 2455991 (**1**) and 2455992 (**2**) contain the supplementary crystallographic data for this paper.[88a,b]

## Acknowledgements

This work was supported by the Conselho Nacional de Desenvolvimento Científico e Tecnológico (CNPq), Fundação de Amparo à Pesquisa do Estado de Minas Gerais (FAPEMIG), Fundação Carlos Chagas Filho de Amparo à Pesquisa do Estado do Rio de Janeiro (FAPERJ), and Fundação de Aperfeiçoamento de Pessoal de Nível Superior (CAPES, Finance Code 001). The Bioanalytical facility NEPS-DQ/UFMG (**https://ne.qui.ufmg.br**), LAREMAR, and LabCri at Universidade Federal de Minas Gerais, are acknowledged for the support in chemical/physical analyses. We thank the Fundação de Amparo à Pesquisa do Estado de São Paulo (FAPESP) for the postdoctoral fellowship ( 2024/00198-0) for RVP, project 2021/08111-2 and for funding the EMU Project 2023/17024-1.

## References

1 R. Marin, G. Brunet and M. Murugesu, Shining New Light on Multifunctional Lanthanide Single–Molecule Magnets, *Angew. Chem., Int. Ed.*, 2021, **60**, 1728–1746.
2 T. L. Mako, J. M. Racicot and M. Levine, Supramolecular Luminescent Sensors, *Chem. Rev.*, 2019, **119**, 322–477.
3 J. J. Zakrzewski, M. Liberka, J. Wang, S. Chorazy and S. Ohkoshi, Optical Phenomena in Molecule-Based Magnetic Materials, *Chem. Rev.*, 2024, **124**, 5930–6050.
4 S. G. McAdams, A.-M. Ariciu, A. K. Kostopoulos, J. P. S. Walsh and F. Tuna, Molecular Single-Ion Magnets Based on Lanthanides and Actinides: Design Considerations and New Advances in the Context of Quantum Technologies, *Coord. Chem. Rev.*, 2017, **346**, 216–239.
5 M. Atzori and R. Sessoli, The Second Quantum Revolution: Role and Challenges of Molecular Chemistry, *J. Am. Chem. Soc.*, 2019, **141**, 11339–11352.
6 E. Moreno-Pineda, Quantum Information Processing with Molecular Magnets, *Phys. B*, 2023, **649**, 414486.
7 E. Moreno-Pineda, C. Godfrin, F. Balestro, W. Wernsdorfer and M. Ruben, Molecular Spin Qudits for Quantum Algorithms, *Chem. Soc. Rev.*, 2018, **47**, 501–513.

 

8 L. Gu and R. Wu, Origin of the Anomalously Low Raman Exponents in Single Molecule Magnets, *Phys. Rev. B: Condens. Matter Mater. Phys.*, 2021, **103**, 014401.
9 N. Ishikawa, M. Sugita, T. Ishikawa, S. Koshihara and Y. Kaizu, Lanthanide Double-Decker Complexes Functioning as Magnets at the Single-Molecular Level, *J. Am. Chem. Soc.*, 2003, **125**, 8694–8695.
10 C. R. Ganivet, B. Ballesteros, G. D. Torre, J. M. Clemente-Juan, E. Coronado and T. Torres, Influence of Peripheral Substitution on the Magnetic Behavior of Single–Ion Magnets Based on Homo– and Heteroleptic TbIII Bis (Phthalocyaninate), *Chem. – Eur. J.*, 2013, **19**, 1457–1465.
11 E. Bartolomé, A. Arauzo, J. Luzón, J. Bartolomé and F. Bartolomé, Magnetic Relaxation of Lanthanide-Based Molecular Magnets, in *Handbook of Magnetic Materials*, ed. E. Brück, Elsevier, 2017, ch. 1, 26, 1–289.
12 V. S. Parmar, D. P. Mills and R. E. P. Winpenny, Mononuclear Dysprosium Alkoxide and Aryloxide Single–Molecule Magnets, *Chem. – Eur. J.*, 2021, **27**, 7625–7645.
13 J. Mayans and A. Escuer, Correlating the Axial Zero Field Splitting with the Slow Magnetic Relaxation in GdIII SIMs, *Chem. Commun.*, 2021, **57**, 721–724.
14 M. Orts-Arroyo, A. Sanchis-Perucho, N. Moliner, I. Castro, F. Lloret and J. Martínez-Lillo, One-Dimensional Gadolinium(III) Complexes Based on Alpha- and Beta-Amino Acids Exhibiting Field-Induced Slow Relaxation of Magnetization, *Inorganics*, 2022, **10**, 32.
15 Y. C. Chen, Y. Y. Peng, J. L. Liu and M. L. Tong, Field-Induced Slow Magnetic Relaxation in a Mononuclear Gd(III) Complex, *Inorg. Chem. Commun.*, 2019, **107**, 107449.
16 S. E. Crawford, P. R. Ohodnicki and J. P. Baltrus, Materials for the Photoluminescent Sensing of Rare Earth Elements: Challenges and Opportunities, *J. Mater. Chem. C*, 2020, **8**, 7975–8006.
17 J. Stefanska, M. Chrunik and L. Marciniak, Sensitivity Enhancement of the Tb $^{3+}$ -Based Single Band Ratiometric Luminescent Thermometry by the Metal-to-Metal Charge Transfer Process, *J. Phys. Chem. C*, 2021, **125**, 5226–5232.
18 J. Drabik, R. Lisiecki and L. Marciniak, Optimization of the Thermometric Performance of Single Band Ratiometric Luminescent Thermometer Based on $Tb^{3+}$ Luminescence by the Enhancement of Thermal Quenching of GSA-Excited Luminescence in TZPN Glass, *J. Alloys Compd.*, 2021, **858**, 157690.
19 D. A. Lima, A. G. Bispo-Jr, D. A. Gálico, S. F. N. Coelho, J. H. Araujo Neto, J. A. Ellena, L. Petiote, I. O. Mazali and F. A. Sigoli, Tuning the Thermometric Features in 1D Luminescent $Eu^{III}$ and $Tb^{III}$ Coordination Polymers through Different Bridge Phosphine Oxide Ligands, *Inorg. Chem.*, 2023, **62**, 6808–6816.
20 C. D. S. Brites, R. Marin, M. Suta, A. N. Carneiro Neto, E. Ximendes, D. Jaque and L. D. Carlos, Spotlight on Luminescence Thermometry: Basics, Challenges, and Cutting–Edge Applications, *Adv. Mat.*, 2023, **35**(36), e2302749.
21 Y. Wu, F. Li, Y. Wu, H. Wang, L. Gu, J. Zhang, Y. Qi, L. Meng, N. Kong, Y. Chai, Q. Hu, Z. Xing, W. Ren, F. Li and X. Zhu, Lanthanide Luminescence Nanothermometer with Working Wavelength beyond 1500 Nm for Cerebrovascular Temperature Imaging in Vivo, *Nat. Commun.*, 2024, **15**, 2341.
22 B. Harrington, Z. Ye, L. Signor and A. D. Pickel, Luminescence Thermometry Beyond the Biological Realm, *ACS Nanosci. Au*, 2024, **4**, 30–61.
23 D. Errulat, R. Marin, D. A. Gálico, K. L. M. Harriman, A. Pialat, B. Gabidullin, F. Iikawa, O. D. D. Couto, J. O. Moilanen, E. Hemmer, F. A. Sigoli and M. Murugesu, A Luminescent Thermometer Exhibiting Slow Relaxation of the Magnetization: Toward Self-Monitored Building Blocks for Next-Generation Optomagnetic Devices, *ACS Cent. Sci.*, 2019, **5**, 1187–1198.
24 T. W. Chamberlain, R. V. Perrella, T. M. Oliveira, P. C. de Sousa Filho and R. I. Walton, A Highly Stable Yttrium Organic Framework as a Host for Optical Thermometry and $D_2O$ Detection, *Chem. – Eur. J.*, 2022, **28**, e202200410.
25 J. Stefanska, M. Chrunik and L. Marciniak, Sensitivity Enhancement of the Tb $^{3+}$ -Based Single Band Ratiometric Luminescent Thermometry by the Metal-to-Metal Charge Transfer Process, *J. Phys. Chem. C*, 2021, **125**, 5226–5232.
26 J. Drabik, R. Lisiecki and L. Marciniak, Optimization of the Thermometric Performance of Single Band Ratiometric Luminescent Thermometer Based on $Tb^{3+}$ Luminescence by the Enhancement of Thermal Quenching of GSA-Excited Luminescence in TZPN Glass, *J. Alloys Compd.*, 2021, **858**, 157690.
27 J. Drabik, R. Kowalski and L. Marciniak, Enhancement of the Sensitivity of Single Band Ratiometric Luminescent Nanothermometers Based on $Tb^{3+}$ Ions through Activation of the Cross Relaxation Process, *Sci. Rep.*, 2020, **10**, 11190.
28 A. Bednarkiewicz, L. Marciniak, L. D. Carlos and D. Jaque, Standardizing Luminescence Nanothermometry for Biomedical Applications, *Nanoscale*, 2020, **12**, 14405–14421.
29 J. Drabik and L. Marciniak, L. $KLaP_4O_{12}$:$Tb^{3+}$ Nanocrystals for Luminescent Thermometry in a Single-Band-Ratiometric Approach, *ACS Appl. Nano Mater.*, 2020, **3**, 3798–3806.
30 W. D. do Pim, W. X. C. Oliveira, M. A. Ribeiro, É. N. de Faria, I. F. Teixeira, H. O. Stumpf, R. M. Lago, C. L. M. Pereira, C. B. Pinheiro, J. C. D. Figueiredo-Júnior, W. C. Nunes, P. P. de Souza, E. F. Pedroso, M. Castellano, J. Cano and M. Julve, A pH-Triggered Bistable Copper(II) Metallacycle as a Reversible Emulsion Switch for Biphasic Processes, *Chem. Commun.*, 2013, **49**, 10778–10780.
31 *CrysAlisPRO, CrysAlis Pro*, Rigaku Oxford Diffraction, Yarnton, Oxfordshire, England, 2018.
32 L. Palatinus and G. Chapuis, SUPERFLIP – a Computer Program for the Solution of Crystal Structures by Charge Flipping in Arbitrary Dimensions, *J. Appl. Crystallogr.*, 2007, **40**, 786–790.
33 G. M. Sheldrick, Crystal Structure Refinement with SHELXL, *Acta Crystallogr., Sect. C: Struct. Chem.*, 2015, **71**, 3–8.

34 L. J. Farrugia, *WinGX* and *ORTEP for Windows*: An Update, *J. Appl. Crystallogr.*, 2012, **45**, 849–854.
35 C. F. Macrae, I. Sovago, S. J. Cottrell, P. T. A. Galek, P. McCabe, E. Pidcock, M. Platings, G. P. Shields, J. S. Stevens, M. Towler and P. A. Wood, Mercury 4.0 : From Visualization to Analysis, Design and Prediction, *J. Appl. Crystallogr.*, 2020, **53**, 226–235.
36 K. Momma and F. Izumi, *VESTA*: A Three-Dimensional Visualization System for Electronic and Structural Analysis, *J. Appl. Crystallogr.*, 2008, **41**, 653–658.
37 R. C. A. Vaz, I. O. Esteves, W. X. C. Oliveira, J. Honorato, F. T. Martins, L. F. Marques, G. L. dos Santos, R. O. Freire, L. T. Jesus, E. F. Pedroso, W. C. Nunes, M. Julve and C. L. M. Pereira, Mononuclear Lanthanide(III)-Oxamate Complexes as New Photoluminescent Field-Induced Single-Molecule Magnets: Solid-State Photophysical and Magnetic Properties, *Dalton Trans.*, 2020, **49**, 16106–16124.
38 R. C. A. Vaz, I. O. Esteves, W. X. C. Oliveira, J. Honorato, F. T. Martins, E. N. da Silva Júnior, D. de C. A. Valente, T. M. Cardozo, B. A. C. Horta, D. L. Mariano, W. C. Nunes, E. F. Pedroso and C. L. M. Pereira, Lanthanide(III)-Oxamato Complexes Containing $Nd^{3+}$ and $Ho^{3+}$ : Crystal Structures, Magnetic Properties, and *Ab Initio* Calculations, *CrystEngComm*, 2022, **24**, 6628–6641.
39 C. R. Araujo Junior, W. X. C. Oliveira, C. B. Pinheiro, E. F. Pedroso, W. C. Nunes, A. A. de Almeida, M. Knobel, M. Julve and C. L. M. Pereira, Crystal Structure and Cryomagnetic Study of a Mononuclear Erbium(III) Oxamate Inclusion Complex, *Acta Crystallogr., Sect. C: Struct. Chem.*, 2024, **80**, 349–356.
40 W. D. do Pim, T. R. G. Simões, W. X. C. Oliveira, I. R. A. Fernandes, C. B. Pinheiro, F. Lloret, M. Julve, H. O. Stumpf and C. L. M. Pereira, Influence of Copper(II) and Nickel(II) Ions in the Topology of Systems Based on a Flexible Bis-Oxamate and Bipyridine Building Blocks, *Cryst. Growth Des.*, 2014, **14**, 5929–5937.
41 W. D. do Pim, É. N. de Faria, W. X. C. Oliveira, C. B. Pinheiro, W. C. Nunes, J. Cano, F. Lloret, M. Julve, H. O. Stumpf and C. L. M. Pereira, A Heterobimetallic $[Mn^{II}_5Cu^{II}_5]$ Nanowheel Modulated by a Flexible Bis-Oxamate Type Ligand, *Dalton Trans.*, 2015, **44**, 10939–10942.
42 W. D. do Pim, T. A. Ribeiro-santos, I. S. Jardim, M. C. M. De Castro, A. H. Braga, M. Gustavo, I. Binatti, H. O. Stumpf, E. Lorençon, M. H. Araujo and C. L. M. Pereira, Bistable Copper(II) Metallosurfactant as Molecular Machine for the Preparation of Hybrid Silica-Based Porous Materials, *Mater. Des.*, 2018, **160**, 876–885.
43 F. J. Caires, L. S. Lima, D. J. C. Gomes, A. C. Gigante and M. Ionashiro, Thermal and Spectroscopic Studies of Solid Oxamate of Light Trivalent Lanthanides, *Thermochim. Acta*, 2013, **569**, 8–16.
44 F. J. Caires, W. D. G. Nunes, C. Gaglieri, A. L. C. S. do Nascimento, J. A. Teixeira, G. A. C. Zangaro, O. Treu-Filho and M. Ionashiro, Thermoanalytical, Spectroscopic and DFT Studies of Heavy Trivalent Lanthanides and Yttrium (III) with Oxamate as Ligand, *Mater. Res.*, 2017, **20**, 937–944.
45 T. T. da Cunha, J. Honorato de Araujo-Neto, M. E. Alvarenga, F. T. Martins, E. F. Pedroso, D. L. Mariano, W. C. Nunes, N. Moliner, F. Lloret, M. Julve and C. L. M. Pereira, Calixarene-like Lanthanide Single-Ion Magnets Based on $Nd^{III}$, $Gd^{III}$, $Tb^{III}$ and $Dy^{III}$ Oxamato Complexes, *Magnetochemistry*, 2024, **10**, 103.
46 A. I. Costa, R. M. R. da Silva, L. D. G. Botelho, S. F. N. Coelho, F. A. Sigoli, J. Honorato, J. Ellena, F. T. Martins, A. M. Gomes, W. C. Nunes, F. Lloret, M. Julve and M. V. Marinho, Intensity and Lifetime Ratiometric Luminescent Thermometer Based on a Tb(III) Coordination Polymer, *Dalton Trans.*, 2024, **53**, 3994–4004.
47 J. W. de Oliveira Maciel, M. A. Lemes, A. K. Valdo, R. Rabelo, F. T. Martins, L. J. Queiroz Maia, R. C. de Santana, F. Lloret, M. Julve and D. Cangussu, Europium (III), Terbium(III), and Gadolinium(III) Oxamato-Based Coordination Polymers: Visible Luminescence and Slow Magnetic Relaxation, *Inorg. Chem.*, 2021, **60**, 6176–6190.
48 S. Kapurwan, A. Mondal, P. K. Sahu and S. Konar, Windmill-like $Ln_4$ Clusters [Ln = Tb(III) and Dy(III)] Bridged by $[\alpha\text{-}AsW_9O_{33}]^{9-}$ Unit Showing Zero-Field SMM Behavior: Experimental and Theoretical Investigation, *Inorg. Chem.*, 2022, **61**, 17459–17468.
49 N. F. Chilton, R. P. Anderson, L. D. Turner, A. Soncini and K. S. Murray, PHI: A Powerful New Program for the Analysis of Anisotropic Monomeric and Exchange-Coupled Polynuclear d - and f -Block Complexes, *J. Comput. Chem.*, 2013, **34**, 1164–1175.
50 C. O. C. da Silveira, W. X. C. Oliveira, E. N. da Silva Júnior, M. E. Alvarenga, F. T. Martins, C. C. Gatto, C. B. Pinheiro, E. F. Pedroso, J. P. O. Silva, L. F. Marques, M. V. Santos, F. R. Torres, R. Euclides, R. O. Freire, W. C. Nunes, A. A. de Almeida, M. Knobel and C. L. M. Pereira, Photoluminescence and Magnetic Properties of Isostructural Europium(III), Gadolinium(III) and Terbium(III) Oxamate-Based Coordination Polymers, *Dalton Trans.*, 2024, **53**, 14995–15009.
51 D. N. Woodruff, R. E. P. Winpenny and R. A. Layfield, Lanthanide Single-Molecule Magnets, *Chem. Rev.*, 2013, **113**, 5110–5148.
52 C. Köhler and E. Rentschler, Functionalized Phosphonates as Building Units for Multi-Dimensional Homo- and Heterometallic 3d-4f Inorganic-Organic Hybrid-Materials, *Dalton Trans.*, 2016, **45**, 12854–12861.
53 R. J. Holmberg, M. A. Polovkova, A. G. Martynov, Y. G. Gorbunova and M. Murugesu, Impact of the Coordination Environment on the Magnetic Properties of Single-Molecule Magnets Based on Homo- and Hetero-Dinuclear Terbium(III) Heteroleptic Tris (Crownphthalocyaninate), *Dalton Trans.*, 2016, **45**, 9320–9327.
54 T. Yoshida, G. Cosquer, D. C. Izuogu, H. Ohtsu, M. Kawano, Y. Lan, W. Wernsdorfer, H. Nojiri, B. K. Breedlove and M. Yamashita, Field-Induced Slow

 

Magnetic Relaxation of GdIII Complex with a Pt–Gd Heterometallic Bond, *Chem. – Eur. J.*, 2017, **23**, 4551–4556.
55 O. Kahn, *Molecular Magnetism*, Wiley – VCH, New York, 1st edn, 1993.
56 K. S. Cole and R. H. Cole, Dispersion and Absorption in Dielectrics I. Alternating Current Characteristics, *J. Chem. Phys.*, 1941, **9**, 341–351.
57 W. J. A. Blackmore, G. K. Gransbury, P. Evans, J. G. C. Kragskow, D. P. Mills and N. F. Chilton, Characterisation of Magnetic Relaxation on Extremely Long Timescales, *Phys. Chem. Chem. Phys.*, 2023, **25**, 16735–16744.
58 C. Rajnák, J. Titiš and R. Boča, Reciprocating Thermal Behavior in Multichannel Relaxation of Cobalt(II) Based Single Ion Magnets, *Magnetochemistry*, 2021, **7**, 76.
59 C. Rajnák and R. Boča, Reciprocating Thermal Behavior in the Family of Single Ion Magnets, *Coord. Chem. Rev.*, 2021, **436**, 213808.
60 C. R. M. O. Matos, C. V. Sarmiento, H. C. Silva, G. B. Ferreira, G. P. Guedes, W. C. Nunes and C. M. Ronconi, Field-Induced Single-Ion Magnets Exhibiting Tri-Axial Anisotropy in a 1D Co(II) Coordination Polymer with a Rigid Ligand 4,4′-(Buta-1,3-Diyne-1,4-Diyl) Dibenzoate, *Dalton Trans.*, 2021, **50**, 15003–15014.
61 R. Boča, C. Rajnák, J. Titiš and D. Valigura, Field Supported Slow Magnetic Relaxation in a Mononuclear Cu (II) Complex, *Inorg. Chem.*, 2017, **56**, 1478–1482.
62 J. Titiš, C. Rajnák, D. Valigura and R. Boča, Field Influence on the Slow Magnetic Relaxation of Nickel-Based Single Ion Magnets, *Dalton Trans.*, 2018, **47**, 7879–7882.
63 R. Boča, C. Rajnák, J. Moncol, J. Titiš and D. Valigura, Breaking the Magic Border of One Second for Slow Magnetic Relaxation of Cobalt-Based Single Ion Magnets, *Inorg. Chem.*, 2018, **57**, 14314–14321.
64 C. Rajnák, J. Titiš, J. Moncol, R. Mičová and R. Boča, Field-Induced Slow Magnetic Relaxation in a Mononuclear Manganese(II) Complex, *Inorg. Chem.*, 2019, **58**, 991–994.
65 M. Gebrezgiabher, S. Schlittenhardt, C. Rajnák, J. Kuchár, A. Sergawie, J. Černák, M. Ruben, M. Thomas and R. Boča, *Triangulo* -{$Er^{III}_3$} Complex Showing Field Supported Slow Magnetic Relaxation, *RSC Adv.*, 2022, **12**, 21674–21680.
66 J. W. Maciel, L. H. G. Kalinke, R. Rabelo, M. E. Alvarenga, F. T. Martins, N. Moliner and D. Cangussu, Slow Relaxation of Magnetization and Magnetocaloric Effects in One-Dimensional Oxamato-Based Lanthanide(III) Coordination Polymers, *Magnetochemistry*, 2025, **11**, 23.
67 J. Wang, Y. Jing, M. Cui, Y. Lu, Z. Ouyang, C. Shao, Z. Wang and Y. Song, Spin Qubit in a 2D $Gd^{III}$ $Na^{I}$ –Based Oxamato Supramolecular Coordination Framework, *Chem. – Eur. J.*, 2023, **24**, e202301771.
68 C.-K. Duan, P. A. Tanner, A. Meijerink and V. Makhov, The Effect of Distortion of the Excited-State Configuration, *J. Phys. Chem. A*, 2011, **115**, 9188–9191.
69 E. B. T. Diogo, E. N. da Silva Júnior, W. X. C. Oliveira, H. O. Stumpf, F. Fabris, A. A. de Almeida, M. Knobel, F. F. Ferreira, W. C. Nunes, E. F. Pedroso, M. Julve and C. L. M. Pereira, Isostructural Oxamate Complexes with Visible Luminescence ($Eu^{3+}$) and Field–Induced Single–Molecule Magnet ($Nd^{3+}$), *Chem. – Asian J.*, 2024, **19**, 202400887.
70 R. M. Abdelhameed, O. M. Darwesh, J. Rocha and A. M. S. Silva, IRMOF–3 Biological Activity Enhancement by Post–Synthetic Modification, *Eur. J. Inorg. Chem.*, 2019, **2019**, 1243–1249.
71 Y. Cui, H. Xu, Y. Yue, Z. Guo, J. Yu, Z. Chen, J. Gao, Y. Yang, G. Qian and B. Chen, A Luminescent Mixed-Lanthanide Metal–Organic Framework Thermometer, *J. Am. Chem. Soc.*, 2012, **134**, 3979–3982.
72 D. A. Gálico, Í. O. Mazali and F. A. Sigoli, A Highly Sensitive Luminescent Ratiometric Thermometer Based on Europium(III) and Terbium(III) Benzoylacetonate Complexes Chemically Bonded to Ethyldiphenylphosphine Oxide Functionalized Polydimethylsiloxane, *New J. Chem.*, 2018, **42**, 18541–18549.
73 A. Vogler and H. Kunkely, Excited State Properties of Lanthanide Complexes: Beyond Ff States, *Inorg. Chim. Acta*, 2006, **359**, 4130–4138.
74 A. D'Aléo, F. Pointillart, L. Ouahab, C. Andraud and O. Maury, Charge Transfer Excited States Sensitization of Lanthanide Emitting from the Visible to the Near-Infra-Red, *Coord. Chem. Rev.*, 2012, **256**, 1604–1620.
75 R. Vieira Perrella, G. Derroso and P. C. de Sousa Filho, Improper Background Treatment Underestimates Thermometric Performance of Rare Earth Vanadate and Phosphovanadate Nanocrystals, *ACS Omega*, 2024, **9**, 34974–34980.
76 F. M. Cabral, D. A. Gálico, I. O. Mazali and F. A. Sigoli, Crystal Structure and Temperature Dependence of the Photophysical Properties of the $[Eu(tta)_3(pyphen)]$ Complex, *Inorg. Chem. Commun.*, 2018, **98**, 29–33.
77 Y. Pan, H.-Q. Su, E.-L. Zhou, H.-Z. Yin, K.-Z. Shao and Z.-M. Su, A Stable Mixed Lanthanide Metal–Organic Framework for Highly Sensitive Thermometry, *Dalton Trans.*, 2019, **48**, 3723–3729.
78 J. Rocha, C. D. S. Brites and L. D. Carlos, Lanthanide Organic Framework Luminescent Thermometers, *Chem. – Eur. J.*, 2016, **22**, 14782–14795.
79 N. F. Mott, On the Absorption of Light by Crystals, *Proc. R. Soc. London, Ser. A*, 1938, **167**, 384–391.
80 F. Seitz, An Interpretation of Crystal Luminescence, *Trans. Faraday Soc.*, 1939, **35**, 74.
81 C. D. S. Brites, A. Millán and L. D. Carlos, Lanthanides in Luminescent Thermometry, in *Handbook on the Physics and Chemistry of Rare Earths*, ed. J. -C. Bünzli and V. K. Pecharsky, Elsevier, 2016, ch. 281, pp. 339–427.
82 S. Katagiri, Y. Hasegawa, Y. Wada and S. Yanagida, Thermo-Sensitive Luminescence Based on the Back Energy Transfer in Terbium(III) Complexes, *Chem. Lett.*, 2004, **33**, 1438–1439.
83 X. Liu, S. Akerboom, M. de Jong, I. Mutikainen, S. Tanase, A. Meijerink and E. Bouwman, Mixed-Lanthanoid Metal–

Organic Framework for Ratiometric Cryogenic Temperature Sensing, *Inorg. Chem.*, 2015, **54**, 11323–11329.
84 C. D. S. Brites, P. P. Lima, N. J. O. Silva, A. Millán, V. S. Amaral, F. Palacio and L. D. Carlos, D. Thermometry at the Nanoscale, *Nanoscale*, 2012, **4**, 4799.
85 K. Trejgis, K. Ledwa, A. Bednarkiewicz and L. Marciniak, A Single-Band Ratiometric Luminescent Thermometer Based on Tetrafluorides Operating Entirely in the Infrared Region, *Nanoscale Adv.*, 2022, **4**, 437–446.
86 J. D. Rinehart and J. R. Long, Exploiting Single-Ion Anisotropy in the Design of f-Element Single-Molecule Magnets, *Chem. Sci.*, 2011, **2**, 2078–2085.
87 A. Dey, P. Kalita and V. Chandrasekhar, Lanthanide(III)-Based Single-Ion Magnets, *ACS Omega*, 2018, **3**, 9462–9475.
88 (*a*) CCDC 2455991: Experimental Crystal Structure Determination, 2025, DOI: **10.5517/ccdc.csd.cc2nfnj9**; (*b*) CCDC 2455992: Experimental Crystal Structure Determination, 2025, DOI: **10.5517/ccdc.csd.cc2nfnkb**.